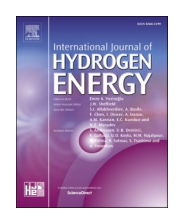
ELSEVIER

Contents lists available at ScienceDirect

# International Journal of Hydrogen Energy

journal homepage: www.elsevier.com/locate/he





# Polymer electrolyte fuel cell operating with nickel foam-based gas diffusion layers: A numerical investigation

Mustafa Ercelik <sup>a,b,\*\*</sup>, Mohammed S. Ismail <sup>c</sup>, Kevin J. Hughes <sup>a,\*</sup>, Derek B. Ingham <sup>a</sup>, Lin Ma <sup>a</sup>, Mohamed Pourkashanian <sup>a,d</sup>

- <sup>a</sup> Energy 2050, Department of Mechanical Engineering, Faculty of Engineering, The University of Sheffield, Sheffield, S3 7RD, United Kingdom
- b Department of Energy Systems Engineering, Faculty of Engineering and Natural Sciences, Iskenderun Technical University, 31200, Iskenderun, Hatay, Turkey
- <sup>c</sup> School of Engineering, University of Hull, Hull, HU6 7RX, United Kingdom
- <sup>d</sup> Translational Energy Research Centre (TERC), University of Sheffield, Sheffield, S9 1ZA, United Kingdom

### ARTICLE INFO

Handling Editor: Ibrahim Dincer

Keywords:
Polymer electrolyte fuel cell
Gas diffusion layer
Nickel foam
Flow channel design
Rib and channel dimensional optimisation
Numerical modelling

### ABSTRACT

Due to their outstanding structural, transport and electrical characteristics, nickel foams serve as excellent candidate materials for gas diffusion layers (GDLs) in polymer electrolyte fuel cells (PEFCs). In this work, a new three-dimensional PEFC model was developed to explore the local and global fuel cell performance with nickel foam-based GDLs. The fuel cell operating with nickel foam GDLs was shown to have, due to its superior mass and charge transport properties, higher oxygen and water concentration and current density compared to that operating with the conventional carbon fibre-based GDLs. The results show that the pumping power should be taken into account when optimising the dimensions of the flow channels and as such the net power density must be the criterion for optimisation. The optimal dimensions of the flow channels for the fuel cell operating with nickel foam based GDLs were found to be 0.25 mm for the channel height and 1 mm for the channel width; the maximum net power density with these dimensions was around 0.95 W/cm² which is two times higher than that operating with carbon fibre based GDLs. All the results have been presented and critically discussed.

# 1. Introduction

The polymer electrolyte fuel cell (PEFC) is a promising clean energy conversion technology that directly converts the chemical energy stored in hydrogen to electrical energy without producing greenhouse gases [1, 2]. The PEFC technology has been employed for transportation applications due to its favourable features: high power density and efficiency, zero-emission, low operating temperature, and compact design [3–6]. A standard PEFC is composed of several key components: (i) a proton-conductive polymeric membrane electrolyte, (ii) anode and cathode catalyst layers where half electrochemical reactions take place, (iii) anode and cathode gas diffusion layers, and (iv) anode and cathode flow field plates.

The gas diffusion layer (GDL) is a wet-proof porous medium that is positioned between the catalyst layer and the flow field plate. The properties of the GDL significantly affect the transport of mass, heat, and electrons between the catalyst layer and the flow field plate [7,8]. A GDL

should ideally fulfil the following functions: (i) supply sufficient oxygen/hydrogen to the catalyst layers, (ii) ease the removal of excess water, (iii) enable fast charge and heat transfer between catalyst layers and flow field plates, and (iv) mechanically support the membrane [9, 10]. The most used form of GDL is carbon paper [11,12]. Nevertheless, the carbon paper-based GDLs are generally susceptible to various forms of degradation including: mechanical degradation, thermal degradation, carbon dissolution, and erosion [13–15]. These degradations detrimentally affect the PEFC performance and lifespan. As a result, more robust GDL materials are required to be developed for PEFC applications.

Metal foams have recently gained significant attention as a prospective GDL material for PEFC applications. This interest stems from their outstanding advantages surpassing conventional carbon fibre-based GDLs. Nickel foam is a promising material for PEFC applications as a GDL and/or flow field plate (FFP) due to its superior electrical and thermal conductivity, high specific surface area, and porous structure.

E-mail addresses: mercelik1@sheffield.ac.uk, mustafaercelik13@gmail.com (M. Ercelik), k.j.hughes@sheffield.ac.uk (K.J. Hughes).

https://doi.org/10.1016/j.ijhydene.2024.05.084

Received 9 January 2024; Received in revised form 9 April 2024; Accepted 6 May 2024 Available online 22 May 2024

<sup>\*</sup> Corresponding author.

<sup>\*\*</sup> Corresponding author. Energy 2050, Department of Mechanical Engineering, Faculty of Engineering, The University of Sheffield, Sheffield, S3 7RD, United Kingdom.

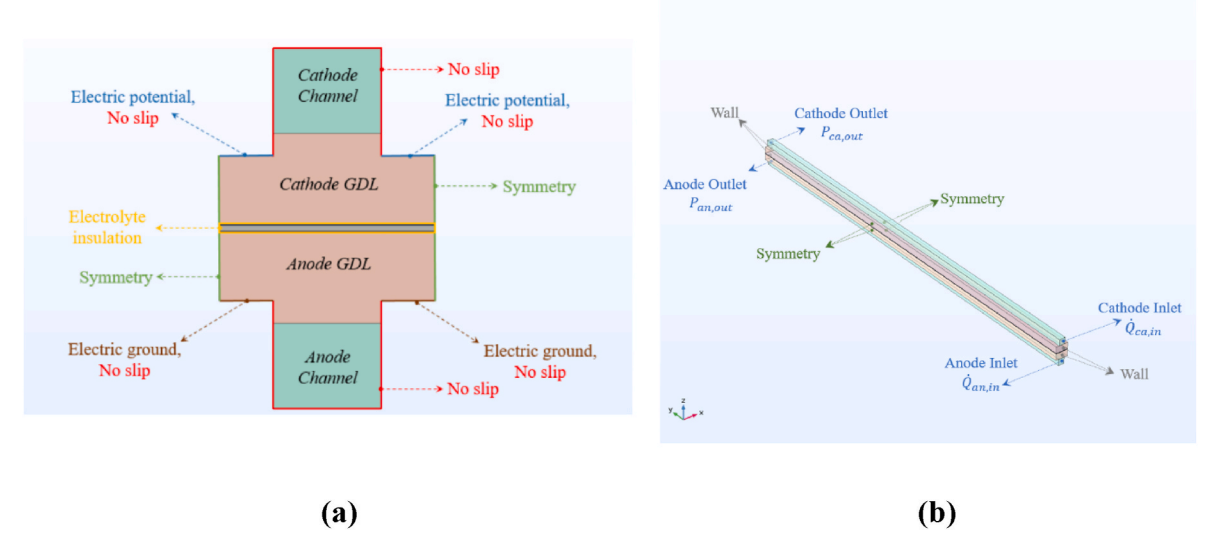


Fig. 1. The PEFC computational domain and the associated boundary conditions: (a) the cross-section and (b) the isometric views.

Shin et al. [16] experimentally compared the nickel foam-based cathode FFP to conventional graphite cathode FFP with serpentine channels. They showed that the nickel foam-based FFP exhibits approximately 50% higher fuel cell performance and more stable operation. Similarly, Tseng et al. [17] evaluated the nickel foam-based cathode FFP in PEFCs. Their results indicated that the nickel foam-based FFP performed better than the conventional graphite-based FFPs. The maximum power density with carbon-based FFP was 0.95 W/cm<sup>2</sup> at 0.5 V, whereas it was 1.35 W/cm<sup>2</sup> with nickel foam-based FFP. This is due to the superior mass transport characteristics of nickel foam-based FFP. Likewise, Tabe et al. [18] conducted an experimental investigation on the nickel foam-based FFP as an alternative to the conventional graphite-based FFPs. Their results showed that the nickel foam-based FFP exhibited better water drainage capability and higher stability than the conventional graphite-based FFPs. Ercelik et al. [19] investigated the structural and transport characteristics of the nickel foam-based GDL using X-ray computed tomography. Their findings revealed that the nickel foam-based GDLs have superior porosity, specific surface area, gas permeability, and effective diffusivity compared to carbon fibre-based GDLs. The same research group [20] evaluated the nickel foam-based GDL under realistic fuel cell compression. They reported that the uncompressed nickel foam sample is almost isotropic and the anisotropy of the nickel foam becomes significantly more profound with increasing compression. Furthermore, their findings indicated that as the compression increases, the mass transport properties decreases and the specific surface area increases. The negative impact on the GDL mass transport properties is less profound with nickel foam than carbon fibre due to the superior transport properties of the former one. In addition, increasing the surface area of the GDL enhances its contact with the catalyst layer and flow field plate, leading to improved electrical and thermal conductivity.

Adequate water management is crucial for PEFCs to achieve high performance and extended lifetime [21,22]. Water is produced at the cathode catalyst layer as a results of the oxygen oxidation reaction (ORR). Furthermore, the reactant and oxidant gases are normally humidified to ensure that the membrane is adequately hydrated, particularly at the start of the fuel cell operation. A portion of the water produced at the cathode may transport to the anode through the membrane due to concentration difference [23]. This mode of transport for dissolved water through the membrane is normally referred to as back diffusion. On the other hand, water at the anode is transported to the cathode through electro-osmotic drag; this may lead to dehydration of the anode side of the membrane. Excess water, especially at the

cathode side, often causes water flooding. This flooding blocks the delivery of reactant gases to the catalyst layer, resulting in performance degradation. Therefore, it is imperative that the GDL materials exhibit a hydrophobic characteristics to facilitate the immediate excess water removal. According to existing literature, nickel foam materials possess superior hydrophobic character when compared to the carbon fibre-based GDLs [24–26]. In addition, the design of the flow channels was, amongst other factors, found to be crucial in removing excess water and maintaining high fuel cell performance [27–30]. The flow channels are grooved into the flow field plates which are conventionally made from graphite. However, metallic flow field plates have been increasingly employed in PEFCs and this is due to the low manufacturing cost, high mechanical strength, being lightweight, and high electrical and thermal conductivity [31].

When designing flow channels, it is vital to optimise both the mass and charge transports. Evidently, wider flow channels allow for better mass transport to/from the catalyst layers, whereas broader ribs enhance electrical conduction between the FFPs and the catalyst layers. Conventional FFPs normally host rectangular cross-section flow channels [32]. However, there have been numerous studies investigating the impact of the design of the flow channel on the fuel cell performance. For example, Khazaee and Sabadbafan [33] numerically investigated three different cross-section designs (rectangular, triangular, and elliptical) for flow channels and they reported that the rectangular cross-section exhibited slightly higher performance at the lower cell voltages. Moreover, for all three cross-section designs, the fuel cell performance was found to significantly improve when the cross-sections increased from 1 to 2 mm<sup>2</sup>. Similarly, Tian et al. [34] investigated the impact of three different flow channel cross-section designs: rectangular, trapezoidal, and hybrid that involves a rectangular inlet and a trapezoidal outlet. They found that the hybrid design demonstrated a higher performance as the gas velocity within the channel increases with this design, thus supplying higher amounts of reactant gases to the catalyst layers through convection. Carcedea et al. [35] created a multiphase and non-isothermal three-dimensional model aiming to assess how the rectangular channel size impacts the PEFC performance. Expectedly, they found that as the channel height or width decrease, the cell performance improves. For instance, when the channel width was reduced from 3 mm to 0.5 mm, there was an 11% increase in the maximum cell power. Higier and Liu [36] experimentally investigated the current density distribution beneath the channel and rib regions and they found that the best-performing FFP channel configuration is that with narrower channels. Their outcome showed that the current density at 0.4 V

**Table 1** Parameters used in the model [20,46–56].

randicters used in the moder [20, 10-30].			
Parameter	Value	Unit	Ref.
Channel length (L)	70	mm	[56]
Channel height (h)	1-0.25	mm	[00]
Channel width (w)	1-0.25	mm	_
Carbon fibre-based GDL height under rib	0.191	mm	[56]
Carbon fibre-based GDL height under rhannel	0.151		
<u> </u>		mm	[56]
Nickel foam-based GDL height under rib	0.63	mm	[20]
Nickel foam-based GDL height under channel	0.84	mm	[20]
Catalyst layer thickness	0.014	mm	[48,49,
Nr. 1	0.051		51,56]
Membrane thickness	0.051	mm	[48,49,
			51,56]
Carbon fibre-based GDL porosity under rib	0.6	-	[47,56]
Carbon fibre-based GDL porosity under	0.7	_	[47,56]
channel			
Nickel foam-based GDL porosity under rib	0.842	_	[20]
Nickel foam-based GDL porosity under	0.866	-	[20]
channel			
Catalyst layer porosity	0.4	-	[48,49,
		_	51,56]
Carbon fibre-based GDL permeability under	$7 \times 10^{-13}$	$m^2$	[47,52]
rib (through-plane)			
Carbon fibre-based GDL permeability under	$3 \times 10^{-13}$	$m^2$	[47,52]
rib (in-plane)			
Carbon fibre-based GDL permeability under	$2  imes 10^{-12}$	$m^2$	[47,52]
channel (through-plane)			
Carbon fibre-based GDL permeability under	$5 \times 10^{-13}$	$m^2$	[47,52]
channel (in-plane)			
Nickel foam-based GDL permeability under	5.6 ×	$m^2$	[20]
rib (through-plane)	$10^{-10}$		
Nickel foam-based GDL permeability under	3.4 ×	$m^2$	[20]
rib (in-plane)	$10^{-10}$		,
Nickel foam-based GDL permeability under	9.7 ×	$m^2$	[20]
channel (through-plane)	$10^{-10}$	***	[20]
Nickel foam-based GDL permeability under	6.9 ×	$m^2$	[20]
channel (in-plane)	$10^{-10}$	***	[20]
Catalyst layer permeability	$1 \times 10^{-12}$	$m^2$	[48,49,
catalyst layer permeability	1 / 10	***	51,56]
Carbon fibre-based GDL electrical	600	S/m	[54]
conductivity under rib (through-plane)	000	<i>5</i> / III	[01]
Carbon fibre-based GDL electrical	5000	S/m	[54]
conductivity under rib (in-plane)	3000	3/111	[34]
Carbon fibre-based GDL electrical	53	S/m	[54]
conductivity under channel (through-	33	3/111	[34]
plane)			
Carbon fibre-based GDL electrical	4000	S/m	[54]
conductivity under channel (in-plane)	4000	3/111	[34]
	E00000	C /	[[0]
Nickel foam-based GDL electrical	500000	S/m	[50]
conductivity under rib (through-plane)	<b>5</b> 00000	0.4	5=03
Nickel foam-based GDL electrical	500000	S/m	[50]
conductivity under rib (in-plane)	470000	0.4	5=03
Nickel foam-based GDL electrical	470000	S/m	[50]
conductivity under channel (through-			
plane)	.=		F= 0.7
Nickel foam-based GDL electrical	470000	S/m	[50]
conductivity under channel (in-plane)			
Catalyst layer electrical conductivity	53	S/m	[49]
Membrane conductivity	10	S/m	[48,49,
			51,56]
Carbon fibre-based GDL thermal conductivity	2	W/	[55]
under rib (through-plane)		(m·K)	
Carbon fibre-based GDL thermal conductivity	33	W/	[55]
under rib (in-plane)		(m·K)	
Carbon fibre-based GDL thermal conductivity	1.27	W/	[55]
under channel (through-plane)		(m·K)	
Carbon fibre-based GDL thermal conductivity	21	W/	[55]
under channel (in-plane)		(m·K)	
Nickel foam-based GDL thermal conductivity	95	W/	[50]
under rib (through-plane)		(m·K)	
Nickel foam-based GDL thermal conductivity	95	W/	[50]
under rib (in-plane)		(m·K)	
Nickel foam-based GDL thermal conductivity	91	W/	[50]
under channel (through-plane)		(m·K)	
Nickel foam-based GDL thermal conductivity	91	W/	[50]
under channel (in-plane)		(m·K)	

Table 1 (continued)

Parameter	Value	Unit	Ref.
Catalyst layer thermal conductivity	0.3	W/	[55]
		(m·K)	
Nickel foam-based GDL effective diffusivity	0.145	cm <sup>2</sup> /s	[20]
under rib (through-plane)			
Nickel foam-based GDL effective diffusivity	0.143	cm <sup>2</sup> /s	[20]
under rib (in-plane)			
Nickel foam-based GDL effective diffusivity	0.152	cm <sup>2</sup> /s	[20]
under channel (through-plane)			
Nickel foam-based GDL effective diffusivity	0.154	cm <sup>2</sup> /s	[20]
under channel (in-plane)			
Diffusivity of oxygen in nitrogen	$2.19 \times$	m <sup>2</sup> /s	[20]
	$10^{-5}$		
Anode catalyst coefficient	0.5	-	[53,56]
Cathode catalyst coefficient	1	-	[53,56]
Relative humidity of inlet gases	90	%	[56]
Oxygen molar ratio in air	0.21	_	[20]
Nitrogen molar ratio in air	0.79	_	[20]
Cell temperature, T	60	°C	[56]
Atmospheric pressure	101325	Pa	[56]
Reference exchange current density at	0.004	$A/m^2$	[51]
cathode			
Reference exchange current density at anode	30	$A/m^2$	[51]
Specific surface area of catalyst layer	$1 \times 10^7$	$m^2/m^3$	[56]
Anode volumetric flow rate	0.1	L/min	[56]
Cathode volumetric flow rate	0.5	L/min	[56]
Faraday's constant, F	96485	C/mol	[51]
Universal gas constant, R	8.314	J/	[55]
		(mol·K)	
Isobaric specific heat capacity of air, cp	1008	J/(kg·K)	[46]
Specific heat ratio of air, k	1.401	_	[46]
Efficiency of compressor, $\eta_{comp}$	70	%	[46]

was approximately 0.6 A/cm<sup>2</sup> for 2 mm channel width, while it was 0.8 A/cm<sup>2</sup> for 1 mm channel width. Likewise, Yoon et al. [37] carried out an experimental study to investigate the effects of channel and rib dimensions. The dimensions of the ribs were varied between 0.5 and 3 mm while keeping the channel width at 1 mm. They found that the fuel cell performance becomes better as the ratio between the areas of the channel and the rib increases. Scholta et al. [38] experimentally found that the ideal width for both the channel and the rib ranged between 0.7 and 1 mm. They also reported that very small channel dimensions are technically challenging and costly. Moreover, very narrow or shallow flow channels may be clogged with water droplets. On the other hand, a channel height of more than 1.5 mm was found to cause a considerable amount of wasted oxygen. Carcedea et al. [39] numerically and experimentally evaluated the influence of the channel dimensions of a large-active-area (200 cm<sup>2</sup>) PEFC. They observed an improvement of up to 7% in the fuel cell peak power density with the smallest channel height (i.e. 0.25 mm); this was attributed to the enhanced removal of excess liquid water.

Kerkoub et al. [40] numerically investigated parallel, serpentine and interdigitated flow configurations with different channel widths (0.4-1.4 mm). They showed that, for all the configurations, the fuel cell performance improves with decreasing channel width (and increasing rib width). As the channel width decreases, the convective flow beneath the ribs increases, leading to higher reactant velocity beneath these ribs and supplying more reactant gases to the catalyst layer. Similar findings were reported by Liu et al. [41]. Kaplan [42] developed a 3D PEFC numerical model to evaluate the effect of the dimensions of rectangular channels on the cell performance. Their results showed that the maximum current density was achieved with a 0.2 mm channel width and a 1 mm channel height due to reduced contact resistance and enhanced oxygen consumption. Chowdhury et al. [43] developed a 3D PEFC isothermal model. They showed that, for a given channel height, the fuel cell performance improves with decreasing channel width. For instance, as the channel width was decreased from 2 mm to 0.25 mm, the current density increased from 0.78 A/cm<sup>2</sup> to 1.05 A/cm<sup>2</sup>. They also highlighted that channel height and width are equally important for the

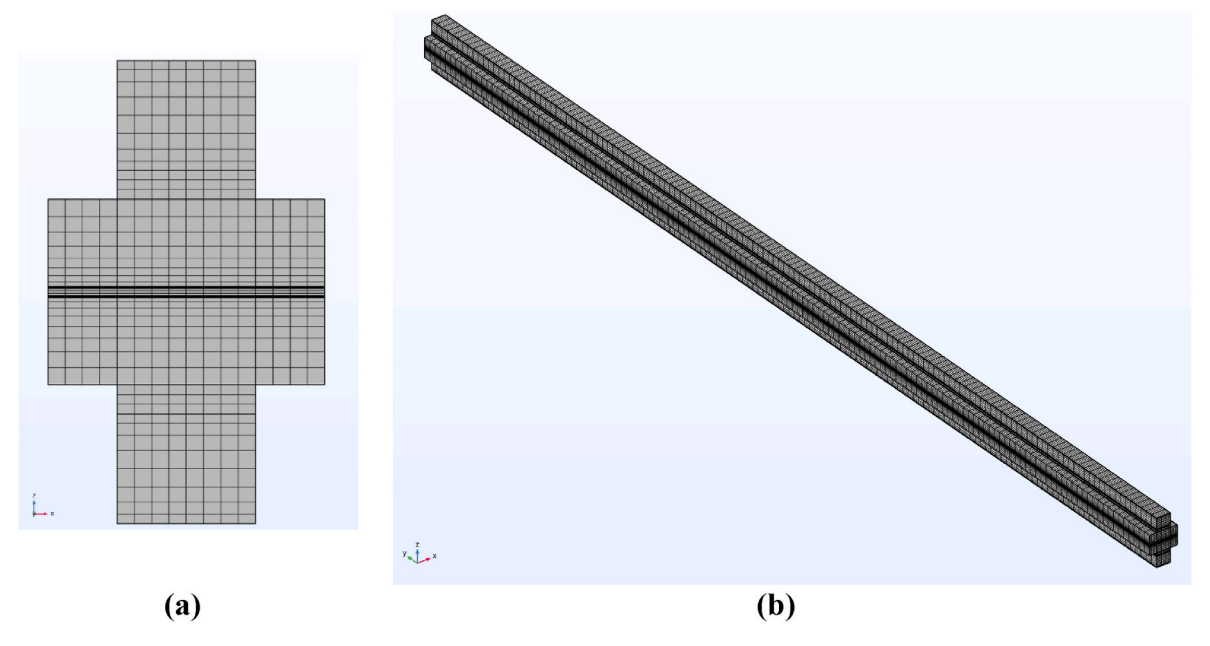


Fig. 2. Nickel foam-based PEFC meshed geometry. (a) The cross section of the meshed geometry and (b) the 3D view of the meshed geometry.

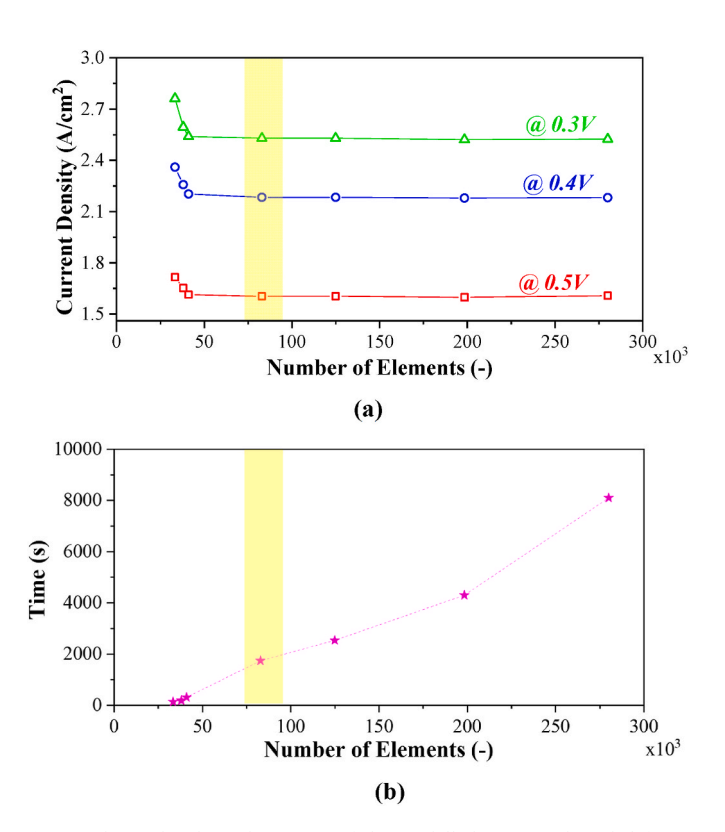
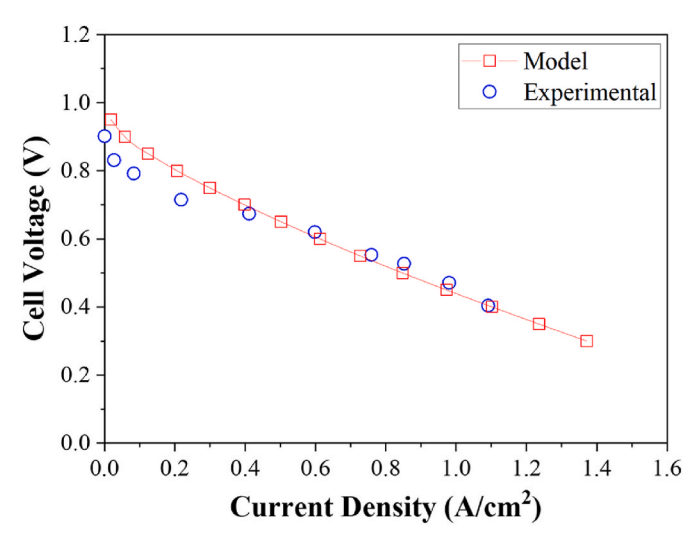


Fig. 3. The grid independency test of the modelled PEFC with nickel foambased GDLs (h = 1 mm, w = 1 mm): (a) the current densities at three different cell voltages and (b) the equivalent computation times. The shaded yellow box shows the selected element numbers. (For interpretation of the references to colour in this figure legend, the reader is referred to the Web version of this article.)

cell performance. In addition, they emphasised that the pumping power must be taken into the account when optimising the dimensions of the channel dimension. Considering both the peak power density and pumping power requirements, the optimal channel dimensions were found to be 1 mm for the channel width and 1 mm for the rib width. This



**Fig. 4.** The simulated polarisation curve for the base as compared with the experimental polarisation curve reported in Ref. [56].

optimised configuration achieved a current density of 0.96 A/cm<sup>2</sup> and 11 Pa pressure drop in the cathode channel. Heidary et al. [44] introduced baffles within the channels to boost mass transport and mitigate water flooding at high current densities. The cell performance was improved by 28% when these baffles were arranged in a staggered configuration rather than in-line configuration. Likewise, Chen et al. [45] developed a two-dimensional numerical model to examine the impact of baffled flow channels on the PEFC performance. They found that the baffles in the channels improved the mass transport and cell performance; however, these baffles caused an increase in the required pumping power. For example, using a solid baffle design resulted in an approximately 25% increase in the cell power density, but the required pumping power increased by at least 35%. To optimise cell performance and minimise pumping power, they proposed introducing small baffles at the start of the channels and transitioning to larger baffles towards the end of the channels. Cooper et al. [46] conducted a comprehensive experimental study to optimise the channel dimensions within a range of 0.25-1 mm. They emphasised the importance of accounting for the

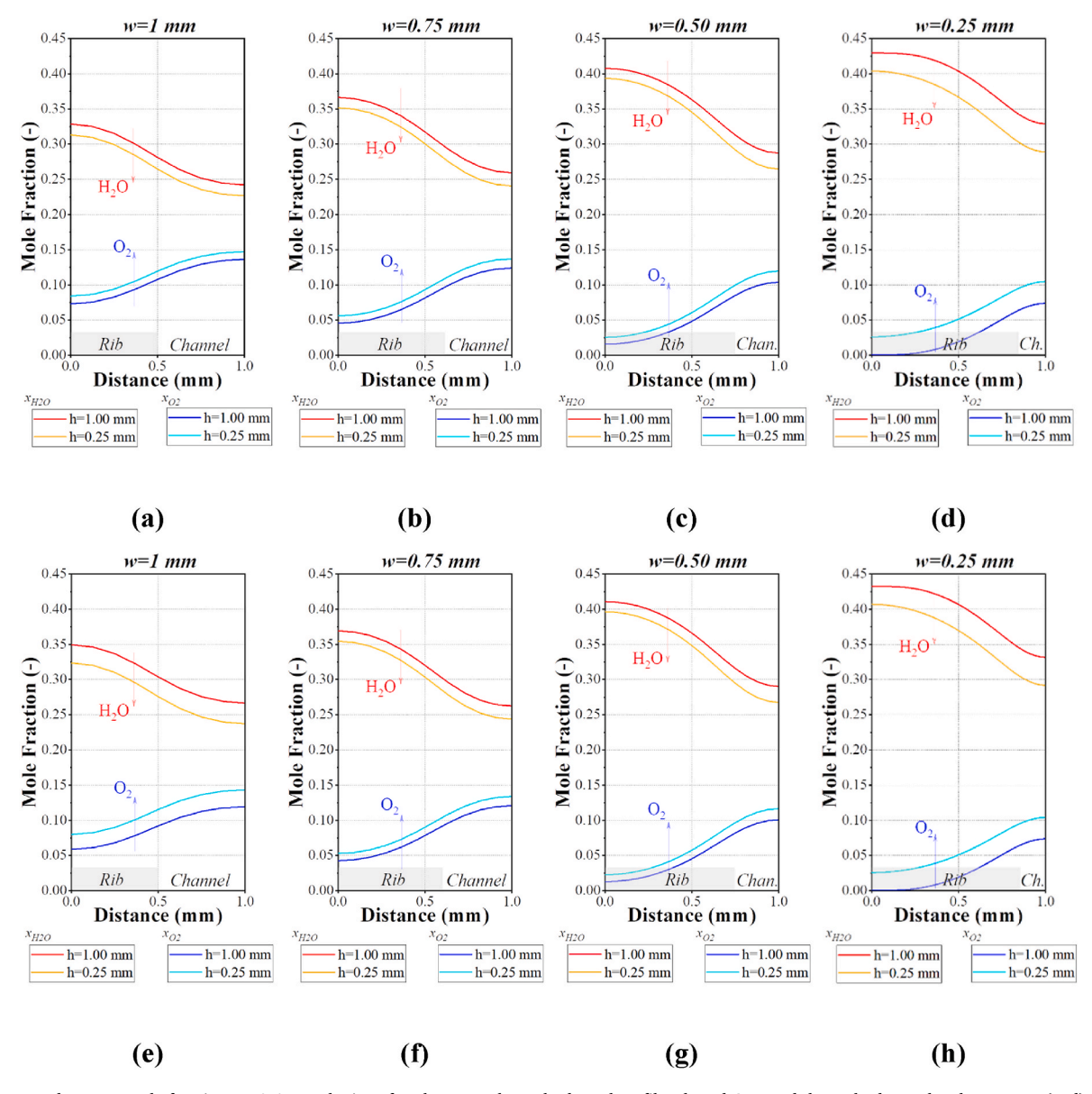


Fig. 5. Water and oxygen mole fractions at 0.4 V at the interface between the cathode carbon fibre-based GDL and the cathode catalyst layer near: (a–d) the inlet (y = 10 mm) and (e–h) the outlet (y = 60 mm) for channel heights 0.25 and 1 mm.

required pumping power when optimising these dimensions. They found that, for the parallel FFP, the peak power density was achieved by a 0.25 mm channel height and a 0.25 mm channel width. Notably, the power densities increased by approximately 40% from 370 W/cm² at a channel height and width of 1 mm to when both dimensions were reduced to 0.25 mm. However, when the required pumping power was taken into consideration, the highest net output power was obtained with a 0.5 mm channel height and a 0.5 mm channel width. For instance, their results indicated that the net power density was 330 W/cm² for a channel height and width of 0.25 mm; however, it increased by approximately 60% at a channel height and width of 0.5 mm.

The above literature survey underscores the crucial role of the channel dimensions in attaining high performance. Due to its superior interior characteristics, nickel foam emerges as a promising material for GDLs in PEFCs; however, there have been no comprehensive PEFC modelling studies focusing on the use of nickel foam as a GDL. This work aims at assessing the performance of PEFC equipped with conventional and nickel foam GDLs. The pressure drop and pumping power required were taken into account when optimising the dimensions of the flow channels. To this end, a three-dimensional PEFC was created to identify

these optimal dimensions.

# 2. Methodology

The geometrical models were constructed using the COMSOL Multiphysics \$ 6.0 software. Fig. 1 depicts the computational domain for the baseline case, where both the channel height and width are set as 1 mm. As shown in the figure, a single straight flow channel has been modelled to save computational time and resources. The following assumptions and considerations were taken into account when developing the current model.

- The operation of the fuel cell is steady state.
- $\bullet$  The flow in the channels is laminar (Re  $\ll$  2300) and incompressible (Ma  $\ll$  0.3).
- The gas mixtures are treated as ideal gases.
- The catalyst layers and membrane are assumed to be isotropic, whereas gas diffusion layers are anisotropic.
- The membrane is impermeable to gases.
- The gas diffusion layer intrusion into the channel is considered.

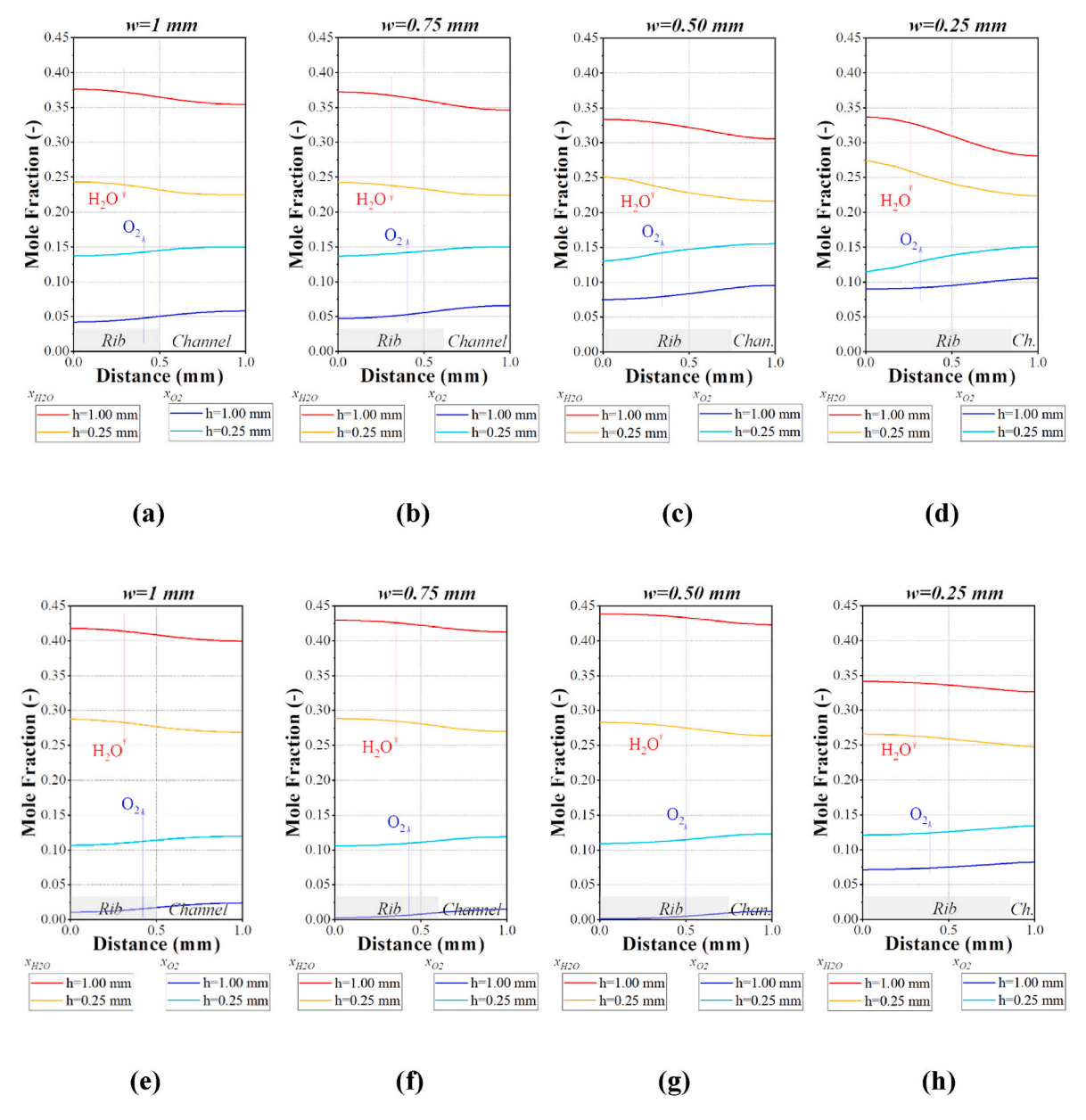


Fig. 6. Water and oxygen mole fractions at 0.4 V at the interface between the cathode nickel foam-based GDL and the cathode catalyst layer near: (a–d) the inlet (y = 10 mm) and (e–h) the outlet (y = 60 mm) for channel heights 0.25 and 1 mm.

 The interfacial contact resistances between components are negligible.

In this study, the channel dimensions were optimised for two different GDL materials: carbon fibre-based and nickel foam-based. A total of 32 scenarios were investigated in this study. The gas diffusion layers were considered 20% compressed under the channel area and 40% compressed under the rib area. The inlet volumetric flow rates on the anode and cathode sides were 0.1 L/min and 0.5 L/min, respectively. The outlet pressure of both anode and cathode flow channels was set to be zero gauge pressure. The symmetrical boundary conditions were defined as shown in Fig. 1. In addition, schematic diagrams of both nickel foam-based and carbon fibre-based PEFCs are presented in Figure S1 in the supplementary material. The model developed is single phase and therefore water only exist in gaseous phase. Table 1 shows the parameters used in the numerical model.

The following set of conservation equations were used in the model [33,57,58]. The conservation of mass is expressed as follows:

$$\nabla(\rho \bullet \mathbf{u}) = S_m \tag{1}$$

where  $\nabla$  is the operator  $\left(i\frac{\partial}{\partial x} + j\frac{\partial}{\partial y} + k\frac{\partial}{\partial z}\right)$ ,  $\rho$  is fluid density (kg/m<sup>3</sup>), u is the velocity vector, and  $S_m$  is the source term. Below is the conservation of momentum equation:

$$\nabla \bullet \left( \frac{\rho \mathbf{u} \mathbf{u}}{\varepsilon^2} \right) = -\nabla P + \nabla \bullet \mu \left[ \left( \nabla \left( \frac{\mathbf{u}}{\varepsilon} \right) + \nabla \left( \frac{\mathbf{u}}{\varepsilon} \right)^T \right) - \frac{2}{3} \nabla \frac{\mathbf{u}}{\varepsilon} \mathbf{I} \right] + S_u$$
 (2)

$$S_u = -\frac{\mu}{\kappa} u \tag{3}$$

where  $\varepsilon$  is porosity of porous medium, P means the pressure, I is the identity matrix,  $\mu$  is the dynamic viscosity (Pa·s), and K is the permeability (m<sup>2</sup>) of the porous media and  $S_u$  is the momentum source term which represent Darcy's law in this case. The porosity of the flow channels is evidently unity. The conservation of species equation is given as:

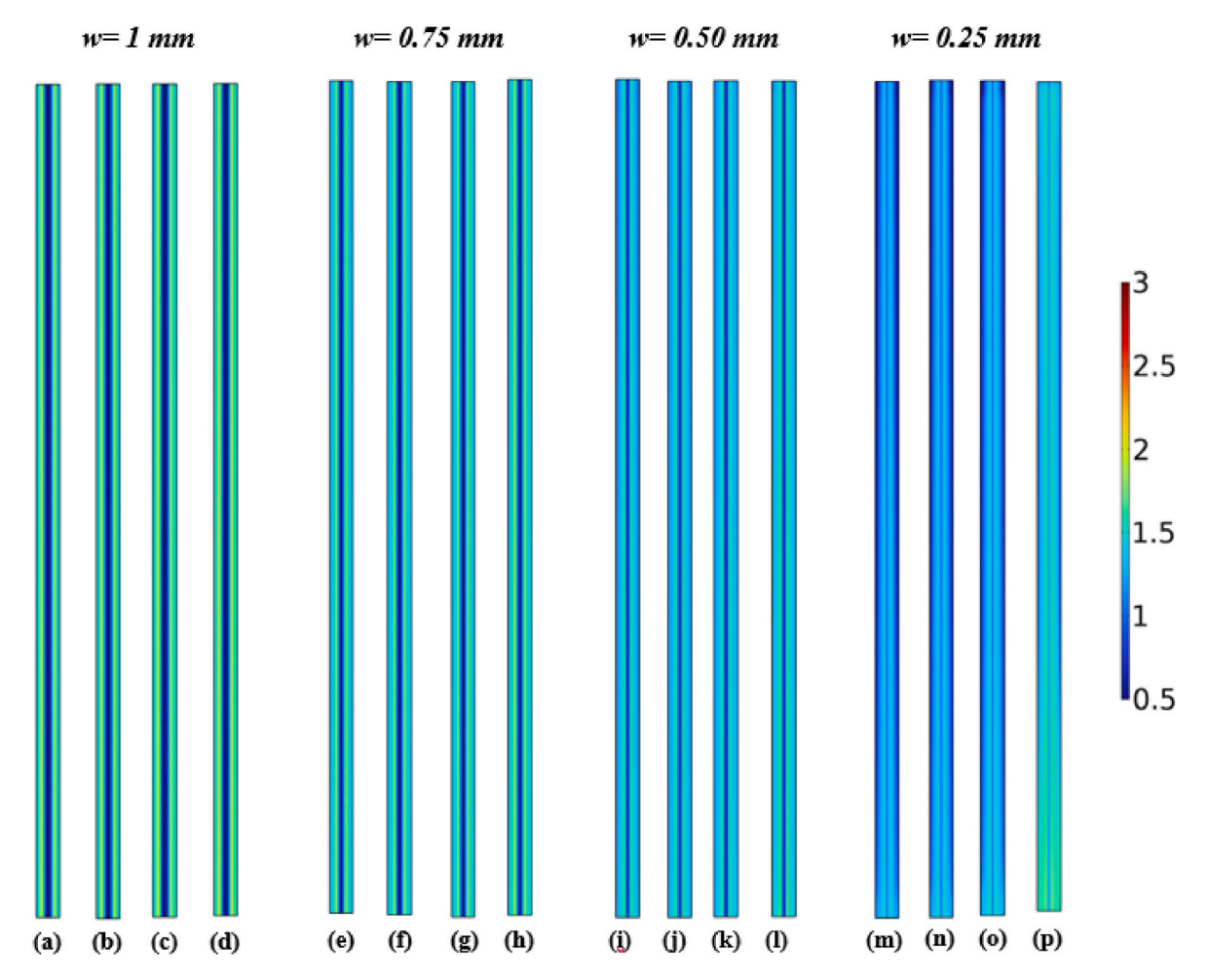


**Fig. 7.** Local current density distributions at the mid-cathode GDL in the carbon fibre-based PEFC at 0.4 V. The distributions are shown for different channel heights: (a, e, i, m) for h = 1 mm; (b, f, j, n) for h = 0.75 mm; (c, g, k, o) for h = 0.5 mm; and (d, h, l, p) for h = 0.25 mm. Note that the inlets are at the bottom of the domains.

$$\nabla \bullet (\rho \mathbf{u} X_k) = \nabla \left( \rho D_k^{eff} X_k \right) + S_k \quad k = O_2, H_2O, H_2$$
 (4)

where  $D_k^{eff}$  is effective mass diffusivity of the species k,  $X_k$  is mass fraction of k, and  $S_k$  is the source term of the species k. The effective diffusivity values of carbon fibre-based GDLs and catalyst layers are calculated using the Bruggeman correlation:

$$D_k^{eff} = \varepsilon^{1.5} D_k \tag{5}$$

where  $\varepsilon$  and  $D_k$  are the porosity of the porous medium and the bulk diffusion coefficient of species k, respectively. It should be noted that the effective diffusivities of nickel foam were taken from the literature [20]. The source terms of species are only applicable in the catalyst layers:

$$S_{H_2} = \frac{-M_{H_2} \, i_a \, a_a}{2F} \tag{6}$$

$$S_{O_2} = \frac{-M_{O_2} i_c a_c}{4F} \tag{7}$$

$$S_{H_2O} = \frac{-M_{H_2O} i_c a_c}{2F}$$
 (8)

where  $M_k$  is molecular weight of species k (kg·mol<sup>-1</sup>) and F is Faraday's constant (96485 C/mol).  $i_a$  and  $i_c$  are the anode and cathode volumetric current densities, respectively.  $a_a$  and  $a_c$  are the anode and cathode specific surface areas, respectively. The conservation of charge is represented by the following equations:

$$\nabla \bullet (-\sigma_{s} \nabla \varphi_{s}) = S_{s} \tag{9}$$

$$\nabla \bullet (-\sigma_l \nabla \varphi_l) = S_l \tag{10}$$

where  $\sigma_s$  and  $\sigma_l$  are electrical conductivities of solid and membrane phases, respectively.  $\varphi_s$  and  $\varphi_l$  represent the solid and membrane phase potentials, respectively.  $S_s$  and  $S_l$  are the charge source terms which are equal to the volumetric transfer current densities at the anode or cathode electrodes. These current densities are obtained from the Butler-Volmer equations:

$$i_{a}a_{a} = i_{a}^{ref} a_{a} \left( \frac{X_{H_{2}}}{X_{H_{2}}^{ref}} \right)^{0.5} \left[ exp \left( \frac{\alpha_{a,a}F}{RT} \eta_{act,a} \right) - exp \left( -\frac{\alpha_{a,c}F}{RT} \eta_{act,c} \right) \right]$$
(11)

$$i_{c}a_{c} = i_{c}^{ref}a_{c}\left(\frac{X_{O_{2}}}{X_{O_{2}}^{ref}}\right) \left[exp\left(\frac{\alpha_{c,a}F}{RT}\eta_{act,c}\right) - exp\left(-\frac{\alpha_{c,c}F}{RT}\eta_{act,c}\right)\right]$$
(12)

where  $i_a^{ref}$  and  $i_c^{ref}$  are the reference current densities at the anode and the cathode, respectively.  $a_a$  and  $a_c$  are the anode and cathode specific surface areas, respectively.  $X_{H_2}^{ref}$  and  $X_{O_2}^{ref}$  represents the hydrogen and oxygen mass fraction at reference conditions (25 °C and 1 atm).  $a_{a,a}$  and  $a_{a,c}$  are anodic and cathodic charge transport coefficient at anode electrode. Likewise,  $a_{c,a}$  and  $a_{c,c}$  are anodic and cathodic charge transport coefficient at cathode electrode. R is the universal gas constant (8.314 J/(mol·K)) and T is the temperature.  $\eta_{act,a}$  and  $\eta_{act,c}$  are anodic and cathodic activation overpotentials:

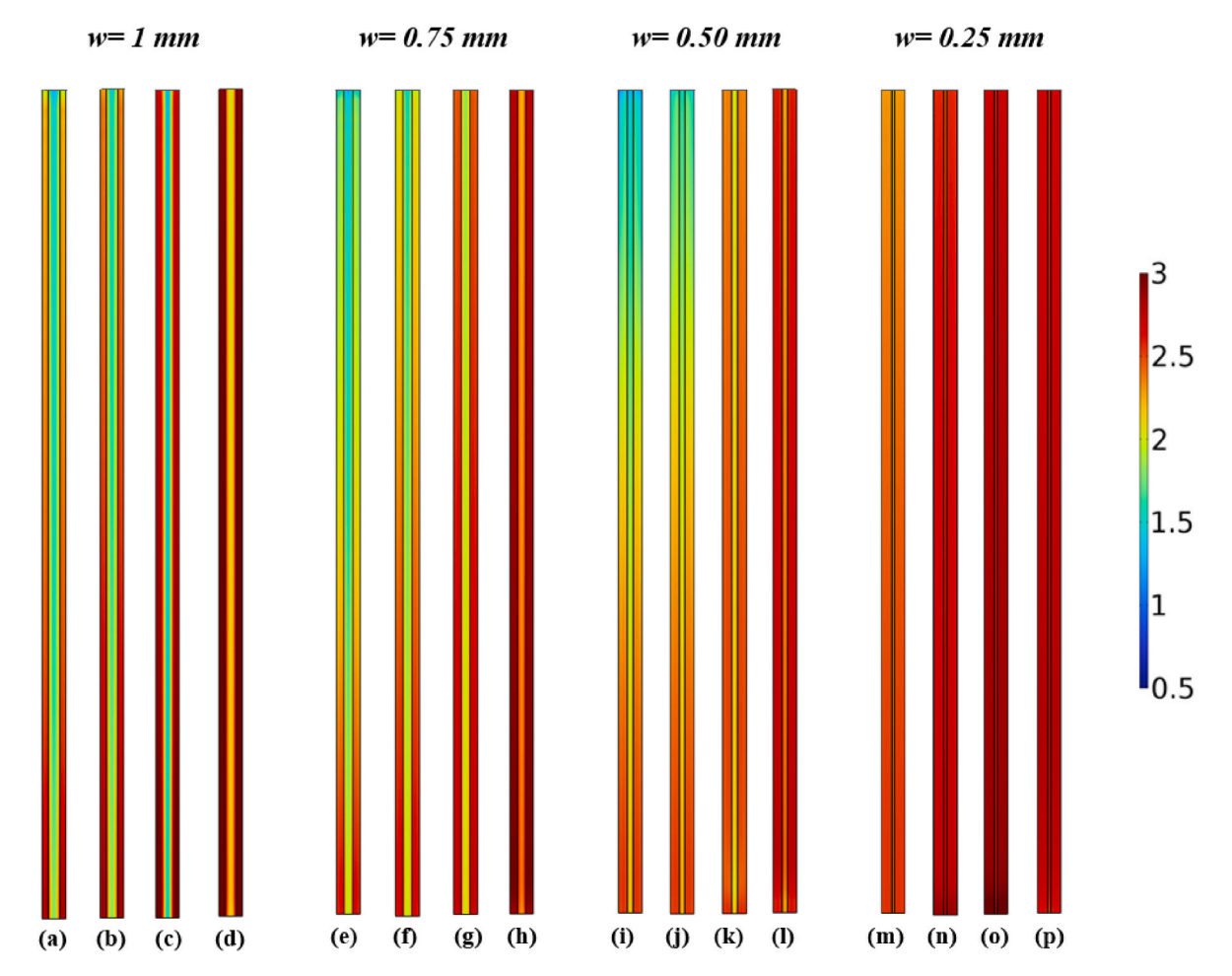


**Fig. 8.** Local current density distributions at the mid-cathode GDL in the nickel foam-based PEFC at 0.4 V. The distributions are shown for different channel heights: (a, e, i, m) for h = 1 mm; (b, f, j, n) for h = 0.75 mm; (c, g, k, o) for h = 0.5 mm; and (d, h, l, p) for h = 0.25 mm. Note that the inlets are at the bottom of the domains.

$$\eta_{act,a} = \varphi_s - \varphi_l \tag{13}$$

$$\eta_{act,c} = \varphi_s - \varphi_l - V_0 \tag{14}$$

where  $V_0$  is the equilibrium cell potential and could be obtained using the following equation [59]:

$$V_0 = 1.482 - 8.45 \times 10^{-4} \ T + 4.31 \times 10^{-5} \ T \ln \left( P_{H_2} \ P_{O_2}^{0.5} \right) \tag{15}$$

The conservation of energy equation is given by:

$$\nabla \bullet (\rho c_p u T) = \nabla \bullet (\lambda \nabla T) + S_T \tag{16}$$

where  $c_p$  is specific heat capacity (J/(kg·K)),  $\lambda$  is thermal conductivity (W/m·K), and  $S_T$  is the heat source term which takes the following forms in the catalyst layer and the membrane, respectively:

$$S_{T,CL} = n \, i + \left(\frac{T\Delta S}{n \, F}\right) i \tag{17}$$

$$S_{T,mem} = \frac{i^2}{\sigma_{mem}} \tag{18}$$

The power required for pumping should be taken into account when computing the net output power needed for the optimisation study, and the cell power density is given by:

$$E_{cell} = i \bullet V \tag{19}$$

and the pumping power density  $(E_{pump})$  is related to the pressure drop

along the flow channel [60]:

$$E_{pump} = \frac{\dot{m}_{air} \bullet c_P \bullet T}{A \bullet \eta_{comp}} \left( \left( \frac{P_{inlet}}{P_{atm}} \right)^{\frac{k-1}{k}} - 1 \right)$$
 (20)

where  $m_{air}$  is the air mass flow rate (kg/s),  $c_P$  is the isobaric specific heat capacity of air (J/(kg·K)), T is the temperature of air (K), A is the cell active area (cm²),  $\eta_{comp}$  is the efficiency of compressor,  $P_{inlet}$  cathode inlet pressure (Pa),  $P_{atm}$  is atmospheric pressure (Pa), and k is the specific heat ratio of air. The required pumping power is directly related to the pressure drop through the flow channel [60]. Therefore, the net power density ( $E_{Net}$ ) is given by:

$$E_{Net} = E_{Cell} - E_{Pump} \tag{21}$$

To ascertain mesh-independent results, the element number has been systematically changed for the base case (h = 1 mm and w = 1 mm) of nickel foam-based GDL analyses. Fig. 2 exhibits the meshed geometry of the base case with nickel foam based GDL. Fig. 3 shows the current density values at cell voltages of 0.3, 0.4, and 0.5 V and the corresponding computation time as they change with the number of elements. The figure shows that, to achieve a mesh-independent solution, the required number of elements is  $\sim$ 80,000 with a computation time of approximately 1800 s. All the numerical simulations were run on a workstation (Intel® Xeon® CPU E5-1650 v4 @ 3.60 GHz) with 192 GB of installed RAM.

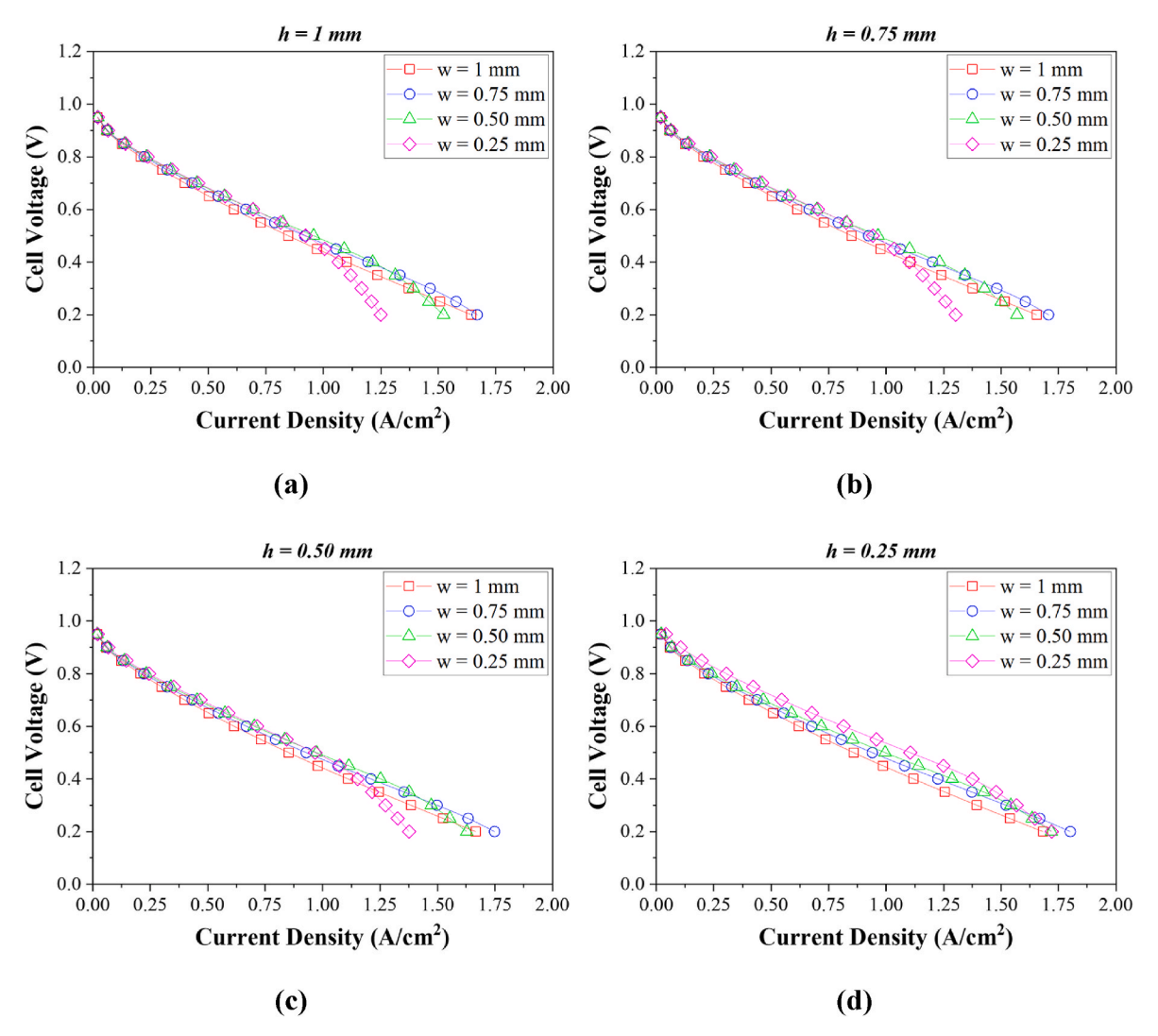


Fig. 9. The polarisation curves of the carbon fibre-based GDL for four different channel widths (w) for (a) 1 mm, (b) 0.75 mm, (c) 0.5 mm, and (d) 0.25 mm channel heights (h).

# 3. Results and discussion

In order to validate the model's accuracy for carbon fibre based PEFC, the results of the base case channel dimensions, h = 1 mm and w = 1 mm, were compared to the experimental results obtained by Wang et al. [56], as shown in Fig. 4. As observed in the figure, the simulated numerical polarisation curve is in good agreement with the experimental results. It should be noted that there is a slight discrepancy of up to 6% between the modelling and the experimental data in the activation losses controlled region lying between 0 and 0.2 A/cm<sup>2</sup>. This could be attributed to the fact that not all the necessary data for the model were provided in Ref. [56] and as such we sourced these missing data from other reliable references, guided by the similarities between the modelled fuel cell and those investigated in these references. Ultimately, this has led to some slight differences between the modelling and experimental data, particularly in the activation losses controlled region. Further, the experimental data shows a slightly steeper decline than the modelling data in the mass transport losses controlled region. This is most likely due the fact that the fuel cell model developed in this study is single phase and therefore the further steepness in the cell voltage at high current densities due to water saturation has not been accurately captured.

# 3.1. Local distributions

A series of numerical simulations were carried out for different channel dimensions ranging from 0.25 mm to 1 mm for carbon fibrebased PEFCs and nickel foam-based PEFCs; note that these ranges are normally used in real-life fuel cells. Fig. 5 show the mole fraction distributions at the cathode catalyst layer/GDL interface for carbon fibrebased PEFC taken near the inlet (y = 10 mm) and the outlet (y = 60mm) for various channel widths at 0.4 V cell voltage for two channel heights: 0.25 and 1 mm. Figures S2 to S6 in the supplementary material display the oxygen and water mole fractions for carbon fibre-based GDLs across all channel heights and widths. As expected, for all the cases, the maximum oxygen concentration and minimum water concentration coincide with the centre of the cathode flow channel. The oxygen concentration diminishes from the centre of the cathode flow channel to the midpoint of the rib, reaching a minimum level; the concentration of water exhibits an opposite trend. Oxygen concentration expectedly decreases from the inlet to the outlet as it is consumed at the catalyst layer, while water concentration increases as it is produced at the catalyst layer. For example, for a channel with width and height both 1 mm (Fig. 5a and e), the oxygen mole fraction drops from 0.136 (at y = 10mm) to 0.119 (at y = 60 mm), and water mole fraction increases from 0.242 to 0.267 at the corresponding locations. Another notable observation is the rise in oxygen concentration and the decline in water

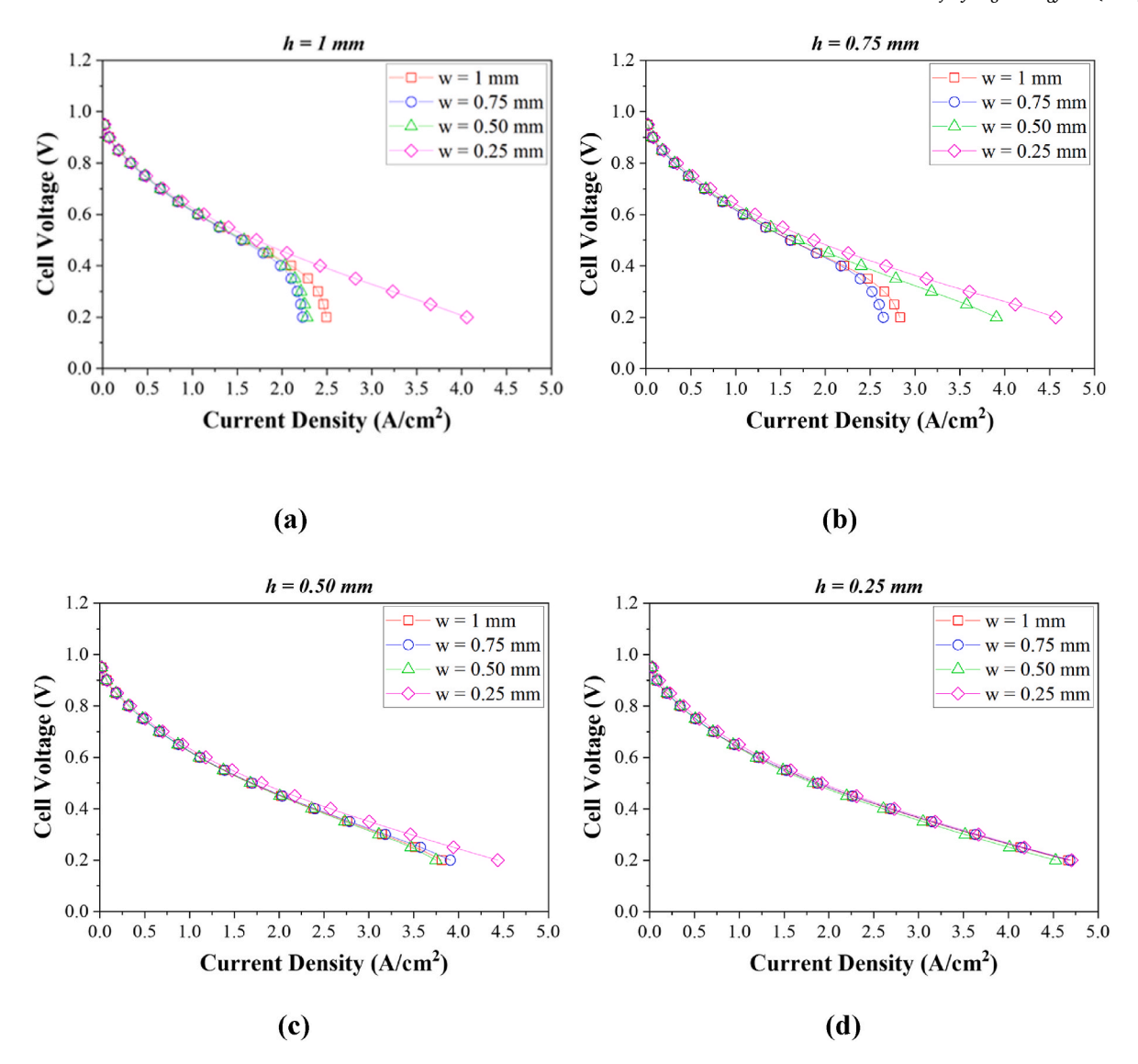


Fig. 10. The polarisation curves of the nickel foam-based GDL for four different channel widths (w) for (a) 1 mm, (b) 0.75 mm, (c) 0.5 mm, and (d) 0.25 mm channel heights (h).

concentration with a decrease in channel height. This is, for a given flow rate, evidently attributed to the increased convective flow within the GDL. Similar trends are maintained for the channel widths 0.75, 0.50 and 0.25 mm. However, the uniformity of oxygen concentration decreases as the channel width decreases. For example, for 1 mm channel width and 1 mm channel height (Fig. 5a and e), moving from the centre of the flow channel to the centre of the rib, the mole fraction of oxygen decreases by 48%. On the other hand, for 0.25 mm channel width and 1 mm channel height (Fig. 5d and h), moving from the centre of flow channel to the centre of the rib, the mole fraction of oxygen decreases by 98%. This is attributed to the widening of the rib as the channel width reduces. Likewise, for all the channel heights, the concentration of oxygen expectedly decreases with decreasing channel width.

Fig. 6 shows the oxygen and water mole fractions at the interface between the cathode catalyst layer and GDL for the nickel foam-based PEFC for the cases where the channel heights are 0.25 and 1 mm. Figures S7 to S11 in the supplementary material display the oxygen and water mole fractions for nickel foam-based GDLs across all channel heights and widths. Notably, for all the cases, the uniformity of oxygen and water concentrations across the flow channel and rib improves with nickel foam based GDLs compared to carbon fibre-based GDLs (this is more profound with shallow flow channels); this is attributed to superior

mass transport properties of the former GDLs [19,20]. For example, near the inlet (y = 10 mm), using nickel foam as a GDL for the case where the channel width is 1 mm and channel height is 0.25 mm, the oxygen mole fraction decreases only by 9% moving from the centre of the channel to the centre of the rib. On the other hand, for the same setting, using carbon fibre-based GDL results in a decrease of 45%. This better uniformity with nickel foam based GDLs is beneficial as it mitigates local oxidant starvation and eases water transport beneath the ribs. One more notable observation is that, compared to the carbon fibre-based GDL, as the channel width decreases, the oxygen concentration increases and water concentration decreases within the cathode GDL. For example, near the outlet (y = 60 mm), for a channel height of 0.25 mm, the oxygen mole fraction under the middle of the rib increases from 0.107 to 0.121 with nickel foam based GDLs when the channel width decreases from 1 to 0.25 mm; however, for the same settings it decreases from 0.812 to 0.003 with carbon fibre-based GDLs. This is due to the flow being more dominated by convection in the case of nickel foam (which has superior gas permeability compared to the conversional GDL [19, 20]) as a result of the nickel foam's significant intrusion into the channels; the intrusion of nickel foam (210  $\mu$ ) into the channels is over three times higher than that of carbon fibre-based GDL (60  $\mu$ ).

Figs. 7 and 8 show the local current density across the flow channel

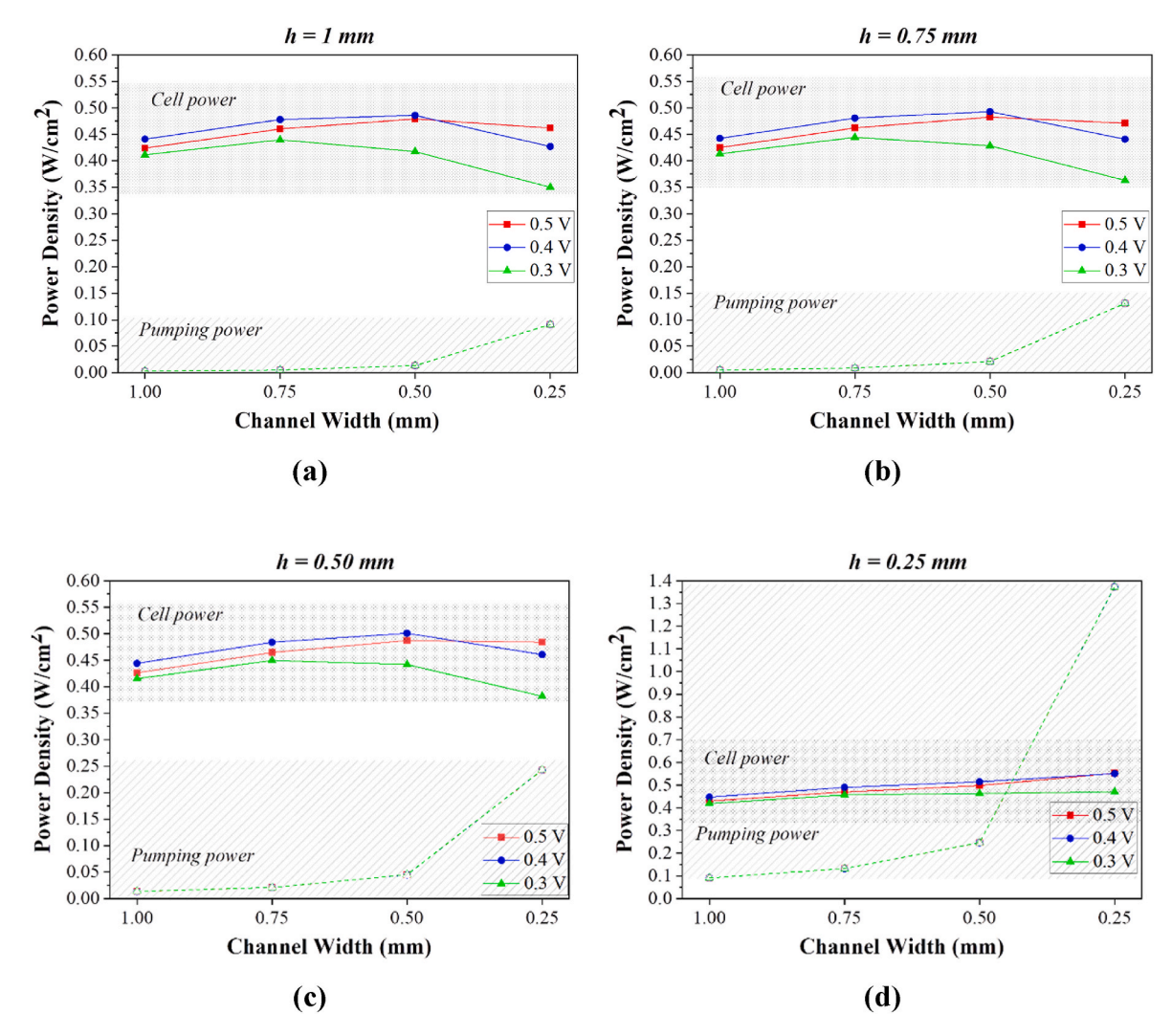


Fig. 11. The cell power density and the pumping power density for the fuel cell equipped with carbon fibre-based GDLs as a function of channel heights ((a) 1 mm, (b) 0.75 mm, (c) 0.5 mm and (d) 0.25 mm) and channel widths.

and the ribs. The first evident observation is that the current density decreases from the inlet to the outlet; this is due to the decreased concentration of oxygen from the inlet to the outlet as a result of its consumption at the catalyst layer. Further, the figure shows that, for all the cases, the current density is a maximum near the edge between the flow channel and the rib as this place is optimal for the combined supply of both the reactant gas and the electrons [59,61]. The figures also show that, for a given channel height, the non-uniformity of current density increases with increasing channel width. This is attributed to the electrons having to travel longer distances to reach the area beneath the centre of the flow channel as the channel width increases. Another observation is that, as the channel height decreases, the uniformity of the current density improves for nickel foam based GDL. This is attributed to the increased convective flows. As with oxygen and water concentrations, Figs. 7 and 8 also show that, for all the cases, the current density is more uniform with a nickel foam based GDL compared to a carbon fibre-based GDL and this is evidently due to the superior mass and charge transport properties of the former GDL [19,20,47].

# 3.2. Polarisation curves

Fig. 9 displays the polarisation curves of the various cases for the fuel cell operating with carbon fibre-based GDLs. The results show that for most of the cases there are optimal channel dimensions that ensure sufficient mass and charge transport and subsequently maximise fuel

cell performance. Specifically, a channel width of 0.50 mm proves to be optimal for most of the channel heights: 1 mm, 0.75 mm, and 0.5 mm. Clearly, this channel width (and the corresponding rib width) ensure adequate mass and charge transport for the above channel heights. However, this is not the case when the channel height is only 0.25 mm as the fuel cell was found to perform better for most of the key regions of the polarisation curve with the minimum channel width: 0.25 mm. This is clearly due to the fact that, for a given flow rate, these small channel dimensions, compared to other configurations, increase the convective flow within the cathode GDL and subsequently ensure supply of adequate amount of oxygen to the catalyst layer.

Fig. 10 shows the polarisation curves of the various cases for the fuel cell operating with nickel foam based GDLs. The first observation is that, for all the cases, the fuel cell with nickel foam based GDLs preform considerably better than with carbon fibre-based GDLs; this is due to the superior mass and charge transport properties demonstrated by the former GDLs [19,20,47]. For example, for the case where the channel width and height are both 1 mm, the limiting current density with carbon fibre-based GDLs is 1.64 A/cm² while it is 2.49 A/cm² with nickel foam based GDLs. The second observation is that the cases where the channel width is 0.25 mm perform better than other cases for most of the channel heights particularly for the channel height of 1 mm. The enhancement in fuel cell performance observed with the 0.25 mm channel width is attributed to the increased convective flow resulting from the reduced cross-sectional area of the channel. Notably, for the 1

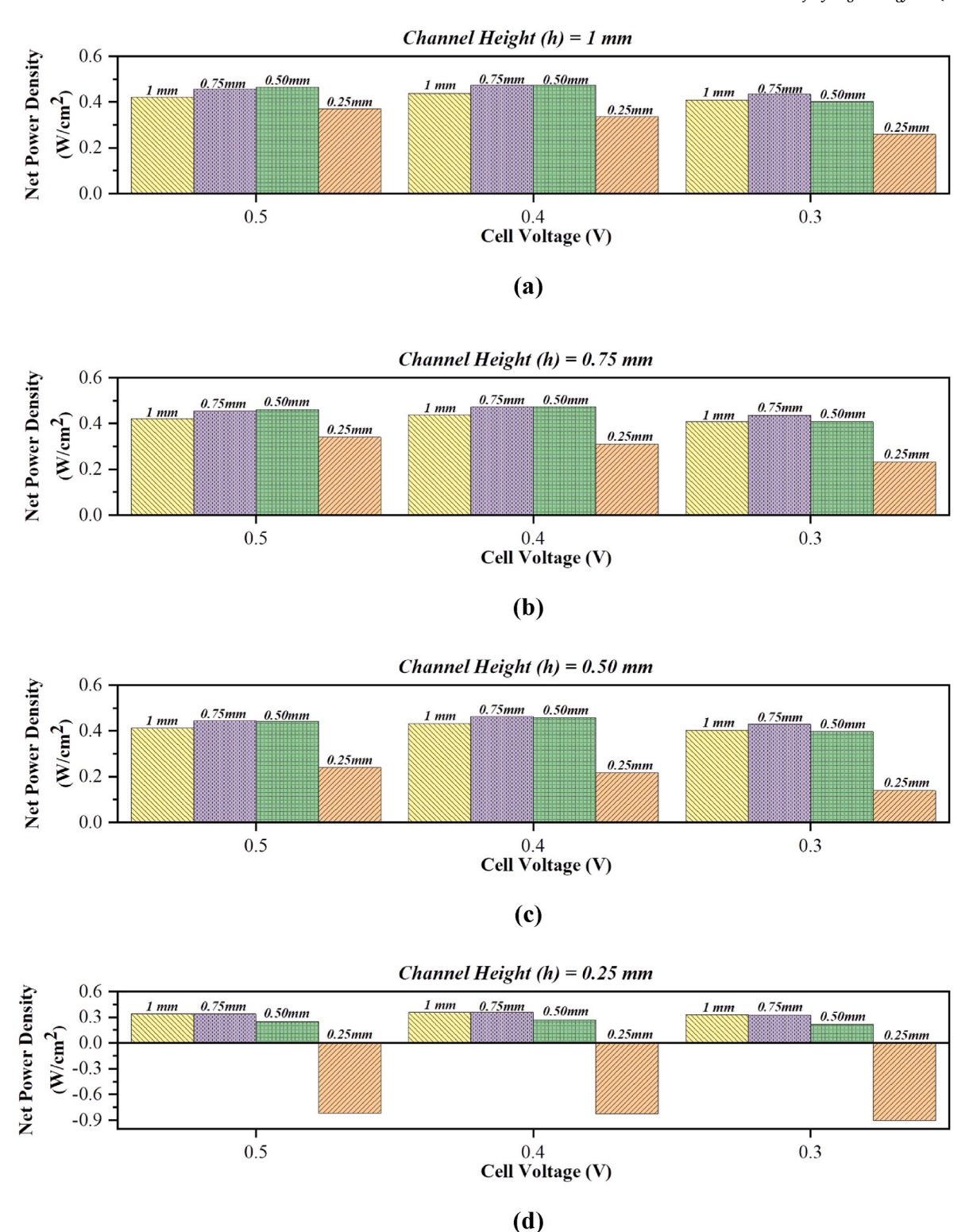


Fig. 12. The net power density for the fuel cell equipped with carbon fibre-based GDLs as a function of channel heights ((a) 1 mm, (b) 0.75 mm, (c) 0.5 mm and (d) 0.25 mm) and channel widths.

mm channel height, the fuel cell with a 1 mm channel width outperforms those with 0.75 mm and 0.50 mm channel widths. The cross-sections of the flow channels with 0.75 mm and 0.50 mm channel widths appear to be not small enough to generate adequately high gas velocities within the nickel foam GDL. It is noteworthy that, in the case of high channel heights, fuel cells employing carbon fibre-based GDLs exhibit improved performance with wider channels in the high current

density region. Conversely, for fuel cells employing nickel foam-based GDLs, except for the 0.25 mm channel height case, the performance improves with narrower channels. This could be explained as follows. The gas permeability of nickel foam-based GDL is higher than that of carbon fibre-based GDLs by 3 orders of magnitude [20], enabling convective flow through it and counterbalancing the reduced contact area between the channel and the GDL. In contrast, the gas permeability

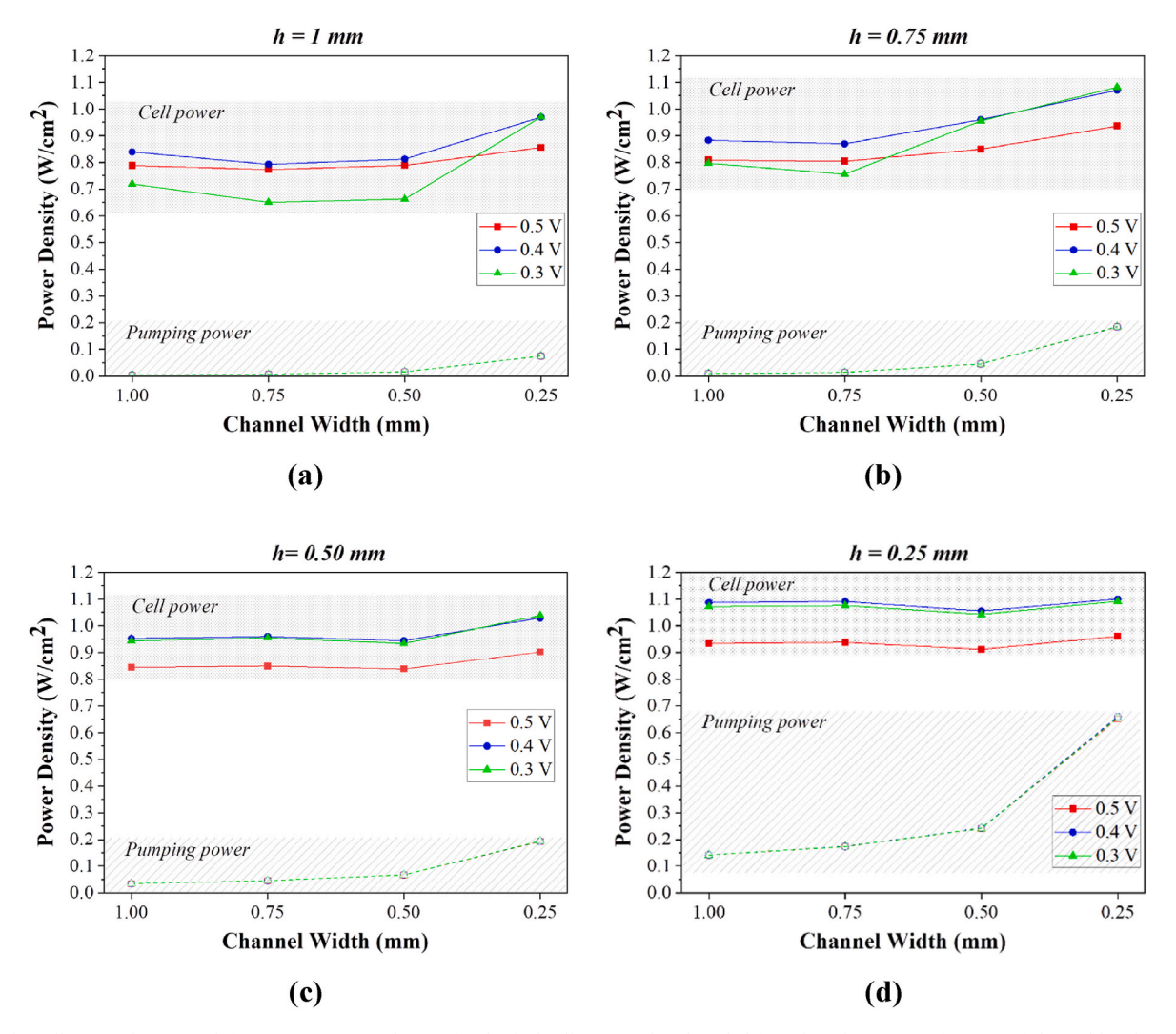


Fig. 13. The cell power density and the pumping power density for the fuel cell equipped with nickel foam-based GDLs as a function of channel heights ((a) 1 mm, (b) 0.75 mm, (c) 0.5 mm and (d) 0.25 mm) and channel widths.

of carbon fibre-based GDLs is not sufficiently high to exploit the increased gas velocity resulting from decreased channel cross-sections. However, in this case, this limitation could be mitigated by increasing the contact areas between the flow channel and the carbon fibre-based GDLs by increasing the width of the channel.

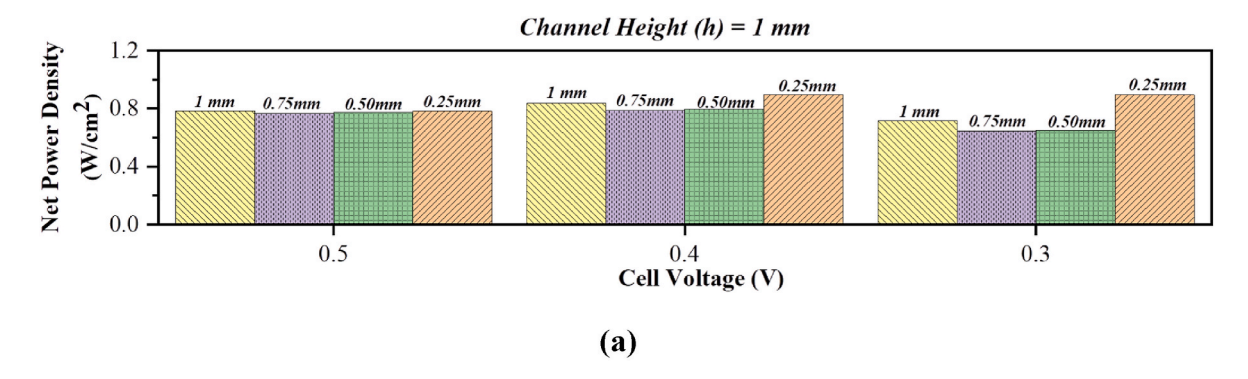
# 3.3. Net output power

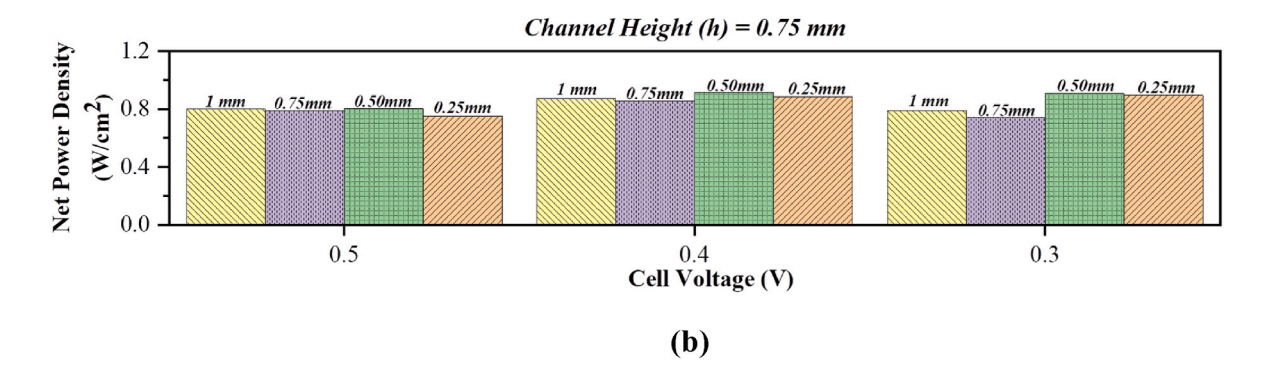
Optimising the fuel cell flow channels involves more than just maximising the fuel cell output power. It is crucial to also take into account the pumping power required to drive the reactant gases through the flow channels during this optimisation process. Fig. 11 presents both the cell power and pumping power densities for the set of channel dimensions investigated in this study for the fuel cell operating with carbon fibre-based GDLs. For most of the cases, the peak cell power density was found to be at 0.4 V. Apart from the cases where the channel height is 0.25 mm, the channel width at which the cell power density is a maximum is 0.5 mm and this is due optimal transport of mass and charge with this setting. However, with 0.25 mm channel height, the cell power density was found to increase with decreasing width of the channel and this is, for a given air flow rate (0.5 L/min), due to increased convective flow within the GDL. However, for this channel height (0.25 mm), the pumping power density increases significantly with decreasing channel width; the pumping power density was found to increase from 0.091 W/ cm<sup>2</sup> with 1 mm channel width to 1.373 W/cm<sup>2</sup> with 0.25 mm channel

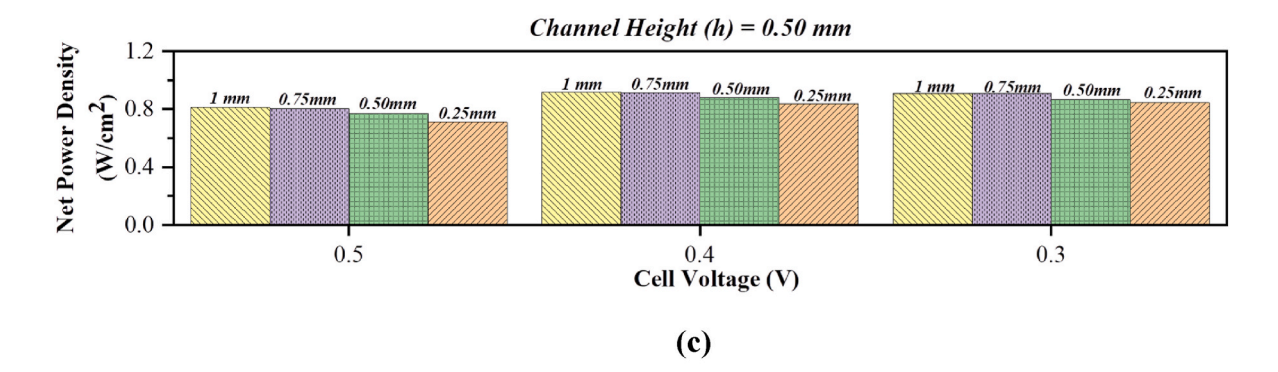
width. On the other hand, the pumping power is minimal with larger channel dimensions. For example, it is only  $0.003~\text{W/cm}^2$  with a channel width and height both set at 1 mm.

Fig. 12 exhibits the net power density, which is the difference between the cell power density and the pumping power density, for all the above cases. The maximum net power density for the fuel cell equipped with carbon fibre-based GDLs is attained at 0.4 V when the channel height is 1 or 0.75 mm and channel width is 0.75 or 0.5 mm, which is around 0.475 W/cm². The pumping power density for these settings is always below 0.05 W/cm². On the other hand, we have negative net power densities for the cases where the channel height is 0.25 mm and the channel width is 0.25 mm. This indicates that the power generated from the fuel cell is not sufficiently high to meet alone the increased pressure drop along the channels and that the pump or the compressor needs an external power source to drive the air through these small cross-sections.

Fig. 13 shows the cell and pumping power densities for the set of channel dimensions investigated in this study for the fuel cell operating with nickel foam based GDLs. As with the fuel cell equipped with the conventional carbon fibre-based GDL, the peak power density for all the cases are attained at 0.4 V cell voltage. The cell power density was, for all the channel heights, found to increase with decreasing channel width. For example, for 1 mm channel height, the cell power density increases by  $0.13 \, \text{W/cm}^2$  when decreasing the channel width from 1 mm to  $0.25 \, \text{mm}$ . This can be attributed to the superior gas permeability of







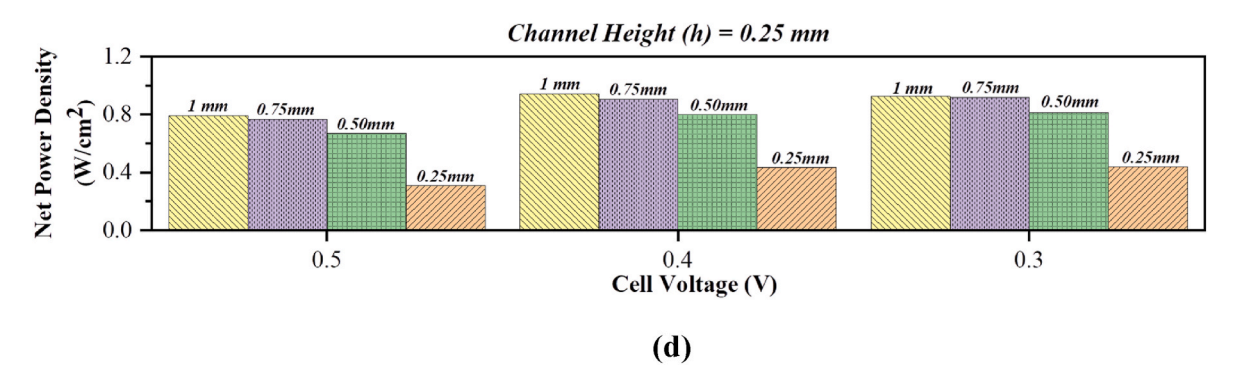


Fig. 14. The net power density for the fuel cell equipped with nickel foam-based GDLs as a function of channel heights ((a) 1 mm, (b) 0.75 mm, (c) 0.5 mm and (d) 0.25 mm) and channel widths.

the nickel foam-based GDLs, leading to increased convective flows within the nickel foam-based GDLs as the flow channel cross-section decreases. The pumping power increases, but to a lesser extent compared to the carbon fibre-based GDLs, as the channel dimensions decrease. For example, the pumping power density increases from 0.004

 $\rm W/cm^2$  with both channel height and width set at 1 mm to 0.660  $\rm W/cm^2$  with both channel height and width set at 0.25 mm.

Fig. 14 displays the net power density for the nickel foam based GDL cases. The maximum net power density,  $0.945~\text{W/cm}^2$ , is achieved at 0.4 V with a channel height of 0.25 mm and a channel width of 1 mm.

Under this channel height, the channel width is adequately high, eliminating the need for significant pumping power. Notably, unlike cases involving carbon fibre-based GDLs, the net power density of the smallest cross-section has not been negative. This is clearly attributed to the superior mass transport properties exhibited by the nickel foam-based GDLs.

#### 4. Conclusions

Nickel foam emerges as a compelling candidate for gas diffusion layers in polymer electrolyte fuel cells due to its superior structural and transport properties. To investigate the performance gain with nickel foam based GDLs, we have developed a three-dimensional PEFC model and simulated different scenarios in which the dimensions of the flow channel were realistically changed with either carbon fibre-based or nickel foam-based GDLs. The following are the main findings of the study.

- The concentrations of oxygen and water as well as current density within the GDL are higher and significantly more uniform with nickel foam GDLs compared to the conventional carbon fibre GDLs and this is due to superior mass and charge transport properties of the nickel foam GDLs. Notably, for all the cases, the maximum current density is near the interface between the flow channel and the rib as this is the location for the shortest pathways for both the reactant gas and the electronic charge.
- The pumping power should be taken into account when optimising the dimensions of the flow channels. The flow channels with the smallest dimension (0.25 mm height and 0.25 mm width) were shown to demonstrate the best fuel cell power density owing to the increased convective flow within the GDL. However, these channels require higher pumping power to overcome the increased pressure drop along the flow channels. For example, for the fuel cell operating with carbon fibre based GDLs, the highest fuel cell power density (0.55 W/cm²) was observed for flow channel with 0.25 mm height and 0.25 mm width. However, the pumping power density was extremely high with these channels (1.373 W/cm²), meaning that the net power density is negative and external power source is required to drive the flow along the channel.
- Taking the pumping power into account, the optimal flow channel dimensions that maximises the net power density (~0.475 W/cm²)

were found to be between 0.75 and 1 mm for the channel height and between 0.5 and 0.75 mm for the channel width for the fuel cell with carbon fibre based GDLs. On the other hand, the maximum net power density optimal flow channel dimensions that maximises the net power density (0.945  $\rm W/cm^2)$ ) were found to be 1 mm for the channel width and 0.25 mm for the channel height for the fuel cell operating with the nickel foam based GDLs. The superior net power density demonstrated with the nickel foam GDLs underscores the superiority of its mass and charge transport properties.

 As a potential future research work, the effects of the interplay between the microporous layer, which is typically coated to the GDL to enhance water management and electrical contact, and various types of GDL is of great interest. Furthermore, comparing the nickel foambased GDL and carbon-fibre-based GDL in terms of durability and cost is an appealing potential future study.

# CRediT authorship contribution statement

Mustafa Ercelik: Conceptualization, Formal analysis, Investigation, Methodology, Software, Validation, Visualization, Writing – original draft, Writing – review & editing. Mohammed S. Ismail: Conceptualization, Formal analysis, Investigation, Methodology, Software, Supervision, Validation, Writing – review & editing. Kevin J. Hughes: Supervision, Writing – review & editing. Derek B. Ingham: Supervision, Writing – review & editing. Lin Ma: Supervision, Writing – review & editing. Mohamed Pourkashanian: Project administration, Supervision, Writing – review & editing.

# Declaration of competing interest

The authors declare that they have no known competing financial interests or personal relationships that could have appeared to influence the work reported in this paper.

# Acknowledgements

The first author, Mustafa Ercelik, would like to thank the Republic of Turkey Ministry of National Education for funding his studentship at the University of Sheffield.

# Appendix A. Supplementary data

Supplementary data to this article can be found online at https://doi.org/10.1016/j.ijhydene.2024.05.084.

# Nomenclature

Symbols		Abbreviations		
A	Cell active area (cm <sup>2</sup> )	CT	Computed tomography	
c <sub>p</sub>	Isobaric specific heat capacity of air (J/(kg·K))	FFP	Flow field plate	
$\hat{D_k}$	Bulk diffusivity of species k (cm <sup>2</sup> /s)	GDL	Gas diffusion layer	
$D_k^{eff}$	Effective diffusivity of the species $k$ (cm <sup>2</sup> /s)	ORR	Oxygen reduction reaction	
$E_{cell}$	Cell power density (W/cm <sup>2</sup> )	PEFC	Polymer electrolyte fuel cell	
$E_{pump}$	Required pumping power density (W/cm <sup>2</sup> )	Subscripts & superscripts		
E <sub>Net</sub>	Net power density (W/cm <sup>2</sup> )	a	Anode	
F	Faraday's constant (C/mol)	air	Air	
h	Channel height (mm)	c	Cathode	
i	Volumetric current densities	cell	Cell	
$\dot{l}_a^{ref}$	Reference current density of anode	comp	Compressor	
$i_c^{ref}$	Reference current density of cathode	eff	Effective	
I	Identity matrix	$H_2$	Hydrogen	
k	Specific heat ratio of air (–)	inlet	Inlet	
K	Permeability (m <sup>2</sup> )	k	Species k	
L	Channel length (mm)	m	Mass	
$\dot{m}_{air}$	Air mass flow rate (kg/s)	mem	Membrane	

(continued on next page)

#### (continued)

$M_k$	Molecular weight of species k (kg⋅mol <sup>-1</sup> )	Net	Net		
P	Pressure (Pa)	outlet	Outlet		
R	Universal gas constant (J/(mol·K))	O <sub>2</sub>	Oxygen		
S	Source term	pump	Pumping		
т	Temperature (°C)	ref	Reference conditions		
1	Velocity (m/s)	u	momentum		
u	Cell voltage (V)	u	momentum		
V	9 1 7				
W	Channel height (mm)				
$X_k$	Mass fraction of species k				
$X_{H_2}^{ref}$	Hydrogen mass fraction at reference conditions				
$X_{O_2}^{ref}$	Oxygen mass fraction at reference conditions				
Greek symbols					
$a_a$	Anode specific surface areas				
$a_c$	Cathode specific surface areas				
$\alpha_{a,a}$	Anodic charge transport coefficient at anode electrode				
$\alpha_{a,c}$	Cathodic charge transport coefficient at anode electrode				
$\alpha_{c,a}$	Anodic charge transport coefficient at cathode electrode				
$\alpha_{c,c}$	Cathodic charge transport coefficient at cathode electrode				
$\varphi_{\scriptscriptstyle S}$	Electrical potentials of solid phase				
$\varphi_l$	Electrical potentials of membrane phase				
ε	Porosity				
μ	Dynamic Viscosity (Pa·s)				
ρ	Fluid density (kg/m <sup>3</sup> )				
λ	Thermal conductivity (W/(m·K))				
$\eta_{comp}$	Efficiency of compressor				
$\eta_{act,a}$	Anodic activation overpotential (V)				
$\eta_{act,c}$	Cathodic activation overpotential (V)				

### References

- Sánchez M, Pierna AR, Lorenzo A, Del Val JJ. Effect of cocatalyst and composition on catalytic performance of amorphous alloys for ethanol electrooxidation and PEMFCs. Int J Hydrogen Energy 2016;41:19749–55. https://doi.org/10.1016/j. iihydene.2016.06.064.
- [2] Aldakheel F, Ismail MS, Hughes KJ, Ingham DB, Ma L, Pourkashanian M. Effects of compression on mechanical integrity, gas permeability and thermal stability of gas diffusion layers with/without sealing gaskets. Int J Hydrogen Energy 2021;46: 22907–19. https://doi.org/10.1016/j.ijhydene.2021.04.087.
- [3] Alaswad A, Baroutaji A, Achour H, Carton J, Al Makky A, Olabi AG. Developments in fuel cell technologies in the transport sector. Int J Hydrogen Energy 2016;41: 16499–508. https://doi.org/10.1016/j.ijhydene.2016.03.164.
- [4] Wang Y, Ruiz Diaz DF, Chen KS, Wang Z, Adroher XC. Materials, technological status, and fundamentals of PEM fuel cells – a review. Mater Today 2020;32: 178–203. https://doi.org/10.1016/j.mattod.2019.06.005.
- [5] Liu Y, Tu Z, Chan SH. Applications of ejectors in proton exchange membrane fuel cells: a review. Fuel Process Technol 2021;214:106683. https://doi.org/10.1016/j. fuproc.2020.106683.
- [6] Orogbemi OM, Ingham DB, Ismail MS, Hughes KJ, Ma L, Pourkashanian M. The effects of the composition of microporous layers on the permeability of gas diffusion layers used in polymer electrolyte fuel cells. Int J Hydrogen Energy 2016; 41:21345–51. https://doi.org/10.1016/j.ijhydene.2016.09.160.
- [7] Zamel N, Li X. Effective transport properties for polymer electrolyte membrane fuel cells - with a focus on the gas diffusion layer. Prog Energy Combust Sci 2013;39: 111–46. https://doi.org/10.1016/j.pecs.2012.07.002.
- [8] Neehall ND, Ismail MS, Hughes KJ, Pourkashanian M. Effect of composition and structure of gas diffusion layer and microporous layer on the through-plane gas permeability of PEFC porous media. Int J Energy Res 2021;45:20988–1005. https://doi.org/10.1002/er.7158.
- [9] Zenyuk IV, Parkinson DY, Connolly LG, Weber AZ. Gas-diffusion-layer structural properties under compression via X-ray tomography. J Power Sources 2016;328: 364–76. https://doi.org/10.1016/j.jpowsour.2016.08.020.
- [10] Colpan CO, Nalbant Y, Ercelik M. Fundamentals of fuel cell technologies. Comprehensive Energy Systems 2018;4–5:1107–30. https://doi.org/10.1016/B978-0-12-809597-3.00446-6.
- [11] Zhao J, Shahgaldi S, Ozden A, Alaefour IE, Li X, Hamdullahpur F. Effect of catalyst deposition on electrode structure, mass transport and performance of polymer electrolyte membrane fuel cells. Appl Energy 2019;255:113802. https://doi.org/ 10.1016/j.apenergy.2019.113802.
- [12] Lee FC, Ismail MS, Ingham DB, Hughes KJ, Ma L, Lyth SM, et al. Alternative architectures and materials for PEMFC gas diffusion layers: a review and outlook. Renew Sustain Energy Rev 2022;166. https://doi.org/10.1016/j. rser.2022.112640.
- [13] Park J, Oh H, Ha T, Lee Y Il, Min K. A review of the gas diffusion layer in proton exchange membrane fuel cells: durability and degradation. Appl Energy 2015;155: 866–80. https://doi.org/10.1016/j.apenergy.2015.06.068.
- [14] Pan Y, Wang H, Brandon NP. Gas diffusion layer degradation in proton exchange membrane fuel cells: mechanisms, characterization techniques and modelling

- approaches. J Power Sources 2021;513:230560.  $\label{eq:https://doi.org/10.1016/j.jpowsour.2021.230560} https://doi.org/10.1016/j.jpowsour.2021.230560.$
- [15] Ozden A, Shahgaldi S, Zhao J, Li X, Hamdullahpur F. Degradations in porous components of a proton exchange membrane fuel cell under freeze-thaw cycles: morphology and microstructure effects. Int J Hydrogen Energy 2020;45:3618–31. https://doi.org/10.1016/j.ijhydene.2018.10.209.
- [16] Shin DK, Yoo JH, Kang DG, Kim MS. Effect of cell size in metal foam inserted to the air channel of polymer electrolyte membrane fuel cell for high performance. Renew Energy 2018;115:663–75. https://doi.org/10.1016/j.renene.2017.08.085.
- [17] Tseng CJ, Tsai BT, Liu ZS, Cheng TC, Chang WC, Lo SK. A PEM fuel cell with metal foam as flow distributor. Energy Convers Manag 2012;62:14–21. https://doi.org/ 10.1016/j.enconman.2012.03.018.
- [18] Tabe Y, Nasu T, Morioka S, Chikahisa T. Performance characteristics and internal phenomena of polymer electrolyte membrane fuel cell with porous flow field. J Power Sources 2013;238:21–8. https://doi.org/10.1016/j. jpowsour.2013.03.047.
- [19] Ercelik M, Ismail MS, Ingham DB, Hughes KJ, Ma L. Efficient X-ray CT-based numerical computations of structural and mass transport properties of nickel foambased GDLs for PEFCs. Energy 2023;262:125531. https://doi.org/10.1016/j. energy.2022.125531.
- [20] Ercelik M, Ismail MS, Hughes KJ, Ingham DB, Ma L, Pourkashanian M. X-ray CT-based numerical investigation of nickel foam-based GDLs under compression. Int J Hydrogen Energy 2023:1–20. https://doi.org/10.1016/j.ijhydene.2023.07.001.
- [21] Okonkwo PC, Otor C. A review of gas diffusion layer properties and water management in proton exchange membrane fuel cell system. Int J Energy Res 2021;45:3780–800. https://doi.org/10.1002/er.6227.
- [22] Lee FC, Ismail MS, Zhang K, Ingham DB, Aldakheel F, Hughes KJ, et al. Optimisation and characterisation of graphene-based microporous layers for polymer electrolyte membrane fuel cells. Int J Hydrogen Energy 2023. https://doi. org/10.1016/j.ijhydene.2023.05.003.
- [23] Ozden A, Shahgaldi S, Li X, Hamdullahpur F. A review of gas diffusion layers for proton exchange membrane fuel cells—with a focus on characteristics, characterization techniques, materials and designs. Prog Energy Combust Sci 2019; 74:50–102. https://doi.org/10.1016/j.pecs.2019.05.002.
- [24] Zhang C, Zhou W, Wang Q, Wang H, Tang Y, Hui KS. Comparison of static contact angle of various metal foams and porous copper fiber sintered sheet. Appl Surf Sci 2013;276:377–82. https://doi.org/10.1016/j.apsusc.2013.03.101.
- [25] Gao R, Liu Q, Wang J, Liu J, Yang W, Gao Z, et al. Construction of superhydrophobic and superoleophilic nickel foam for separation of water and oil mixture. Appl Surf Sci 2014;289:417–24. https://doi.org/10.1016/j. apsusc 2013 10 178
- [26] Aldakheel F, Ismail MS, Hughes KJ, Ingham DB, Ma L, Pourkashanian M, et al. Gas permeability, wettability and morphology of gas diffusion layers before and after performing a realistic ex-situ compression test. Renew Energy 2020;151:1082–91. https://doi.org/10.1016/j.renene.2019.11.109.
- [27] Ozden A, Ercelik M, Ouellette D, Colpan CO, Ganjehsarabi H, Hamdullahpur F. Designing, modeling and performance investigation of bio-inspired flow field based DMFCs. Int J Hydrogen Energy 2017;42:21546–58. https://doi.org/10.1016/j.ijhydene.2017.01.007.

- [28] Ouellette D, Ozden A, Ercelik M, Colpan CO, Ganjehsarabi H, Li X, et al. Assessment of different bio-inspired flow fields for direct methanol fuel cells through 3D modeling and experimental studies. Int J Hydrogen Energy 2018;43: 1152–70. https://doi.org/10.1016/j.ijhydene.2017.06.073.
- [29] Tang Y, Yuan W, Pan M, Wan Z. Feasibility study of porous copper fiber sintered felt: a novel porous flow field in proton exchange membrane fuel cells. Int J Hydrogen Energy 2010;35:9661–77. https://doi.org/10.1016/j. ijhydene.2010.06.101.
- [30] Ismail MS, Berber MR, Alrowaili ZA, Pourkashanian M. Fully-developed laminar flow in trapezoidal ducts with rounded corners: a numerical solution and case study. Int J Numer Methods Heat Fluid Flow 2022;32:2682–99. https://doi.org/ 10.1108/HFF-09-2021-0620.
- [31] Wilberforce T, Ijaodola O, Baroutaji A, Ogungbemi E, Olabi AG. Effect of bipolar plate material on proton exchange membrane fuel cell performance. Energies 2022;15:1–15. https://doi.org/10.3390/en15051886.
- [32] Kumar A, Reddy RG. Modeling of polymer electrolyte membrane fuel cell with metal foam in the flow-field of the bipolar/end plates. J Power Sources 2003;114: 54–62. https://doi.org/10.1016/S0378-7753(02)00540-2.
- [33] Khazaee I, Sabadbafan H. Numerical study of changing the geometry of the flow field of a PEM fuel cell. Heat and Mass Transfer/Waerme- Und Stoffuebertragung 2016;52:993–1003. https://doi.org/10.1007/s00231-015-1621-4.
- [34] Tian J, Ismail MS, Ingham D, Hughes KJ, Ma L, Pourkashanian M. Multiphase, three-dimensional PEM fuel cell numerical model with a variable cross-sectional area flow channel. Int J Numer Methods Heat Fluid Flow 2023;33:2778–99. https://doi.org/10.1108/HFF-02-2023-0075.
- [35] Carcadea E, Varlam M, Ingham DB, Ismail MS, Patularu L, Marinoiu A, et al. The effects of cathode flow channel size and operating conditions on PEM fuel performance: a CFD modelling study and experimental demonstration. Int J Energy Res 2018;42:2789–804. https://doi.org/10.1002/er.4068.
- [36] Higier A, Liu H. Optimization of PEM fuel cell flow field via local current density measurement. Int J Hydrogen Energy 2010;35:2144–50. https://doi.org/10.1016/ i.iihydene.2009.12.116.
- [37] Yoon YG, Lee WY, Park GG, Yang TH, Kim CS. Effects of channel and rib widths of flow field plates on the performance of a PEMFC. Int J Hydrogen Energy 2005;30: 1363–6. https://doi.org/10.1016/j.ijhydene.2005.04.008.
- [38] Scholta J, Escher G, Zhang W, Küppers L, Jörissen L, Lehnert W. Investigation on the influence of channel geometries on PEMFC performance. J Power Sources 2006;155:66–71. https://doi.org/10.1016/j.jpowsour.2005.05.099.
- [39] Carcadea E, Ismail MS, Ingham D Bin, Patularu L, Schitea D, Marinoiu A, et al. Effects of geometrical dimensions of flow channels of a large-active-area PEM fuel cell: a CFD study. Int J Hydrogen Energy 2021;46:13572–82. https://doi.org/ 10.1016/j.ijhydene.2020.08.150.
- [40] Kerkoub Y, Benzaoui A, Haddad F, Ziari YK. Channel to rib width ratio influence with various flow field designs on performance of PEM fuel cell. Energy Convers Manag 2018:174:260–75. https://doi.org/10.1016/j.enconman.2018.08.041.
- [41] Liu H, Li P, Wang K. Optimization of PEM fuel cell flow channel dimensions mathematic modeling analysis and experimental verification. Int J Hydrogen Energy 2013;38:9835–46. https://doi.org/10.1016/j.ijhydene.2013.05.159.
- [42] Kaplan M. Numerical investigation of influence of cross-sectional dimensions of flow channels on pem fuel cell performance. Journal of Energy Systems 2021;5: 137–48. https://doi.org/10.30521/jes.871018.
- [43] Chowdhury MZ, Genc O, Toros S. Numerical optimization of channel to land width ratio for PEM fuel cell. Int J Hydrogen Energy 2018;43:10798–809. https://doi. org/10.1016/j.ijhydene.2017.12.149.
- [44] Heidary H, Kermani MJ, Advani SG, Prasad AK. Experimental investigation of inline and staggered blockages in parallel flowfield channels of PEM fuel cells. Int J Hydrogen Energy 2016;41:6885–93. https://doi.org/10.1016/j. iihydene.2016.03.028.

- [45] Chen H, Guo H, Ye F, Ma CF, Liao Q, Zhu X. Mass transfer in proton exchange membrane fuel cells with baffled flow channels and a porous-blocked baffled flow channel design. Int J Energy Res 2019;43:2910–29. https://doi.org/10.1002/ cr.4461
- [46] Cooper NJ, Smith T, Santamaria AD, Park JW. Experimental optimization of parallel and interdigitated PEMFC flow-field channel geometry. Int J Hydrogen Energy 2016;41:1213–23. https://doi.org/10.1016/j.ijhydene.2015.11.153.
- [47] Zenyuk IV, Parkinson DY, Connolly LG, Weber AZ. Gas-diffusion-layer structural properties under compression via X-ray tomography. J Power Sources 2016;328: 364–76. https://doi.org/10.1016/j.jpowsour.2016.08.020.
- [48] Mahmoudimehr J, Daryadel A. Influences of feeding conditions and objective function on the optimal design of gas flow channel of a PEM fuel cell. Int J Hydrogen Energy 2017;42:23141–59. https://doi.org/10.1016/j. iihydene.2017.07.196.
- [49] Mahmoudimehr J, Darbandi A. Technical study of a PEM fuel cell on the Psychrometric chart. Int J Hydrogen Energy 2016;41:607–13. https://doi.org/ 10.1016/j.ijhydene.2015.10.123.
- [50] Poserin V, Marcuson S, Shu J, Wilkinson DS. CVD technique for Inco nickel foam production. Adv Eng Mater 2004;6:454–9. https://doi.org/10.1002/ adem 200405142
- [51] Akbari MH, Rismanchi B. Numerical investigation of flow field configuration and contact resistance for PEM fuel cell performance. Renew Energy 2008;33:1775–83. https://doi.org/10.1016/j.renene.2007.10.009.
- [52] Taira H, Liu H. In-situ measurements of GDL effective permeability and under-land cross-flow in a PEM fuel cell. Int J Hydrogen Energy 2012;37:13725–30. https://doi.org/10.1016/j.ijhydene.2012.03.030.
- [53] Son J, Um S, Kim YB. Numerical analysis of the effect of anisotropic gas diffusion layer permeability on polymer electrolyte membrane fuel cell performance with various channel types. Fuel 2021;289:119888. https://doi.org/10.1016/j. firel\_2020\_119888
- [54] Nitta I, Hottinen T, Himanen O, Mikkola M. Inhomogeneous compression of PEMFC gas diffusion layer. Part I. Experimental. J Power Sources 2007;171:26–36. https://doi.org/10.1016/j.jpowsour.2006.11.018.
- [55] He G, Yamazaki Y, Abudula A. A three-dimensional analysis of the effect of anisotropic gas diffusion layer(GDL) thermal conductivity on the heat transfer and two-phase behavior in a proton exchange membrane fuel cell(PEMFC). J Power Sources 2010;195:1551–60. https://doi.org/10.1016/j.jpowsour.2009.09.059.
- [56] Wang L, Husar A, Zhou T, Liu H. A parametric study of PEM fuel cell performances. Int J Hydrogen Energy 2003;28:1263–72. https://doi.org/10.1016/S0360-3199 (02)00284-7.
- [57] Azarafza A, Ismail MS, Rezakazemi M, Pourkashanian M. Comparative study of conventional and unconventional designs of cathode flow fields in PEM fuel cell. Renew Sustain Energy Rev 2019;116:109420. https://doi.org/10.1016/j. rser.2019.109420.
- [58] Kwon OJ, Shin HS, Cheon SH, Oh BS. A study of numerical analysis for PEMFC using a multiphysics program and statistical method. Int J Hydrogen Energy 2015; 40:11577–86. https://doi.org/10.1016/j.jihydene.2015.03.163, Elsevier Ltd.
- [59] Ismail MS, Hughes KJ, Ingham DB, Ma L, Pourkashanian M. Effects of anisotropic permeability and electrical conductivity of gas diffusion layers on the performance of proton exchange membrane fuel cells. Appl Energy 2012;95:50–63. https://doi. org/10.1016/j.apenergy.2012.02.003.
- [60] Wang Y. Porous-media flow fields for polymer electrolyte fuel cells. J Electrochem Soc 2009;156:B1124. https://doi.org/10.1149/1.3183781.
  [61] Wang J, Zhang H, Cai W, Ye W, Tong Y, Cheng H. Effect of varying rib area
- [61] Wang J, Zhang H, Cai W, Ye W, Tong Y, Cheng H. Effect of varying rib area portions on the performance of PEM fuel cells: insights into design and optimization. Renew Energy 2023;217:119185. https://doi.org/10.1016/j. renene.2023.119185.